Title: PI(3,5)P_2 Controls the Signaling Activity of Class I PI3K

Authors: Jiachen Sun[1], Seohyeon Song[2], Indira Singaram[1], Ashutosh Sharma[1], Wei Wang[1], Yusi Hu[1], Wen-Ting Lo[3], Philipp Alexander Koch[3], Jean J. Zhao[4], Volker Haucke[3], Ruixuan Gao[1], and Wonhwa Cho[1,*]

[1]*Departments of Chemistry, University of Illinois Chicago, Chicago, IL 60607, USA*

[2]*Division of Integrative Biosciences and Biotechnology, Pohang University of Science and Technology, Pohang, 790-784, Korea*

[3]*Leibniz-Forschungsinstitut für Molekulare Pharmakologie (FMP), 13125 Berlin, Germany*

[4]*Department of Cancer Biology, Dana-Farber Cancer Institute, Boston, MA 02215*

**Corresponding author: Wonhwa Cho, Department of Chemistry, University of Illinois Chicago, Chicago, IL 60607, USA;* E-mail: wcho@uic.edu; Phone: 312-996-4883; FAX: 312-996-0431.

Keywords: PI(3,5)P_2, PI3K regulation, p85, SH2 domain, PI3KC2β, PIKfyve

ABSTRACT

3'-Phosphoinositides are ubiquitous cellular lipids that play pivotal regulatory roles in health and disease. Generation of 3'-phosphoinositides are driven by three families of phosphoinositide 3-kinases (PI3K) but the mechanisms underlying their regulation and cross-talk are not fully understood. Among 3'-phosphoinositides, phosphatidylinositol-3,5-bisphosphate (PI(3,5)P_2) remains the least understood species in terms of its spatiotemporal dynamics and physiological function due to the lack of specific probes. By means of spatiotemporally resolved *in situ* quantitative imaging of PI(3,5)P_2 using a newly developed ratiometric PI(3,5)P_2 sensor we demonstrate that a special pool of PI(3,5)P_2 is generated on lysosomes and late endosomes in response to growth factor stimulation. This PI(3,5)P_2 pool, the formation of which is mediated by Class II PI3KC2β and PIKFyve, plays a crucial role in terminating the activity of growth factor-stimulated Class I PI3K, one of the most frequently mutated proteins in cancer, via specific interaction with its regulatory p85 subunit. Cancer-causing mutations of Class I PI3K inhibit the p85-PI(3,5)P_2 interaction and thereby induce sustained activation of Class I PI3K. Our results unravel a hitherto unknown tight regulatory interplay between Class I and II PI3Ks mediated by PI(3,5)P_2, which may be important for controlling the strength of PI3K-mediated growth factor signaling. These results also suggest a new therapeutic possibility of treating cancer patients with p85 mutations.

INTRODUCTION

Phosphoinositides (PtdInsPs) are phosphorylated derivatives of phosphatidylinositol that play critical roles in cellular signaling and membrane trafficking (Balla, 2013; Di Paolo and De Camilli, 2006; Posor et al., 2022). 3'-PtdInsPs consist of PI(3)P, PI(3,5)P_2, phosphatidylinositol-3,4-bisphosphate (PI(3,4)P_2), and phosphatidylinositol-3,4,5-triphosphate (PIP_3) that are metabolically linked through lipid kinases and phosphatases (Marat and Haucke, 2016). In response to cell activation by growth factors and other stimuli, Class I PI3K converts phosphatidylinositol-4,5-bisphosphate (PI(4,5)P_2) in the plasma membrane (PM) to PIP_3, from which PI(3,4)P_2 is generated by 5'-PtdInsP phosphatases (Bilanges et al., 2019; Fruman et al., 2017; Goulden et al., 2019; Liu et al., 2018) (Burke et al., 2022), including SHIP2. PI(3,4)P_2 can be also produced from phosphatidylinositol-4-phosphate (PI4P) by Class II PI3K (Braccini et al., 2015; Burke et al., 2022; Li Chew et al., 2015; Posor et al., 2013). PIP_3 and PI(3,4)P_2 activate diverse downstream signaling pathways, most notably Akt signaling (Bilanges et al., 2019; Fruman et al., 2017). PI(3)P, which is generally known to be involved in membrane trafficking, is generated primarily in endosomes from phosphatidylinositol (PI) by Class II or Class III PI3K (Schink et al., 2013). It can be also produced from PI(3,4)P_2 by the 4'-PtdInsP phosphatase INPP4. PI(3,5)P_2 has been reported to be synthesized exclusively by PIKFyve from PI(3)P on endolysomal membranes and is involved in membrane trafficking and cell signaling (Burke et al., 2022; Hasegawa et al., 2017; Rivero-Ríos and Weisman, 2022). PIKFyve and PI(3,5)P_2 have gained much attention lately as PIKFyve-specific inhibitors, Apilimod in particular, have emerged as promising drug candidates for cancer, neurodegenerative diseases (Burke et al., 2022; Rivero-Ríos and Weisman, 2022), and COVID-19 (Riva et al., 2020). Compared to other 3'-PtdInsPs, however, the spatiotemporal cellular distribution and dynamics of PI(3,5)P_2 have remained elusive due to the lack of a robust PI(3,5)P_2 probe. In general, PtdInsPs operate by recruiting effector proteins to defined membrane sites where they regulate the cellular activities of these proteins (Balla, 2013; Di Paolo and De Camilli, 2006; Posor et al., 2022). To date, only a limited number of proteins have been reported to bind PI(3,5)P_2 (Rivero-Ríos and Weisman, 2022) and even for those reported (Li et al., 2013; Vines et al., 2022), their specificity for PI(3,5)P_2 remains controversial (Hammond et al., 2015; Hasegawa et al., 2017), which has hampered development of a PI(3,5)P_2-specific biosensors. The lack of a reliable PI(3,5)P_2 biosensor has made it difficult to determine the exact cellular functions of PI(3,5)P_2 in health and disease.

It has been generally thought that three classes of PI3Ks, which are central players in complex 3'-PtdInsP signaling pathways, have independent functions and regulatory mechanisms (Bilanges et al., 2019; Fruman et al., 2017). Although some recent studies have suggested the presence of cross-talks and inter-dependence of their signaling pathways, the interplay among three classes of PI3Ks in health and disease is not fully understood. In particular, little is known about the potential involvement of Class II and III PI3Ks and their products, most notably PI(3)P and PI(3,5)P_2, in regulation of Class I PI3K, the most mutated protein in human breast cancer (Bilanges et al., 2019; Fruman et al., 2017). To address these critical mechanistic questions, we have developed new PI(3)P and PI(3,5)P_2-specific ratiometric sensors that allow *in situ* quantification of PI(3)P and PI(3,5)P_2, respectively, in living cells. Spatiotemporally resolved lipid quantification and enzyme activity measurements reveal a hitherto unknown feedback inhibition mechanism in which a special pool of PI(3,5)P_2, generated by PIKFyve from a special pool of PI(3)P produced by Class II PI3KC2β, terminates the growth factor-stimulated Class I PI3K activity by interacting with the Src-homology 2 (SH2) domains of its regulatory p85 subunit. Our results also show that many hot-spot oncogenic mutations in the p85 subunit of Class I PI3K induce sustained activation of Class I PI3K by weakening the inhibitory p85-PI(3,5)P_2 interaction.

RESULTS

The C-terminal SH2 domain of p85 specifically binds PI(3,5)P_2

The Src homology 2 (SH2) domain is a prototypal protein interaction domain that specifically recognizes the phosphotyrosine (pY) motif of diverse target molecules (Lim and Pawson, 2010; Liu and Nash, 2012; Pawson, 2004). Through genome-wide screening we recently showed that most human SH2 domains tightly and specifically bind lipids in the PM, including PtdInsPs, (Park et al., 2016), which is crucial for the enzymatic activity and scaffolding function of their host proteins (Kim et al., 2018; Sheng et al., 2016; Singaram et al., 2022).

Through surface plasmon resonance (SPR)-based screening (Chen et al., 2012; Park et al., 2016) of >500 lipid binding domains, including 85 human SH2 domains, we conducted a comprehensive search for PI(3,5)P_2-binding proteins and discovered that the C-terminal SH2 domains (cSH2) of the regulatory p85α and p85β subunits of Class I PI3K bound PI(3,5)P_2-containing large unilamellar vesicles (LUVs) with high affinity and specificity. Both p85α-cSH2 and p85β-cSH2 prefer PI(3,5)P_2 over other PtdInsPs in vesicles (**Fig. 1A** and **Fig. S1A**). The N-

terminal SH2 domains of p85α and p85β (p85-nSH2) also bound PI(3,5)P_2 but unlike p85-cSH2 they did not display strong PI(3,5)P_2 selectivity (**Fig. S1B**). The K_d values for p85-cSH2-membrane binding (**Fig. S1C** and **Table S1**) show that p85α-cSH2 has five-fold higher affinity for PI(3,5)P_2-containing LUVs than for PI(4,5)P_2 vesicles. The PI(3,5)P_2 affinity of p85α-cSH2 (i.e., $K_d \approx 200$ nM) is comparable to that reported for binding of canonical lipid binding domains to their cognate lipids (Cho and Stahelin, 2005). Since p85α-cSH2 had ca. 3-times higher membrane affinity than p85β-cSH2 (**Table S1**), we focused our further analysis on p85α-cSH2.

Electrostatic and surface cavity analysis (Park et al., 2016) of p85α-cSH2 predicted that a potential PI(3,5)P_2 binding site of p85α-cSH2 is formed by a cationic pocket that is topologically distinct from the pY-binding pocket (**Fig. 1B**). Molecular docking analysis of p85α-cSH2-PI(3,5)P_2 also suggested that the pocket could accommodate a PI(3,5)P_2 headgroup with the side chain of K653 making energetically favorable interactions with the 3'-phosphate groups of the PI(3,5)P_2 molecule (**Fig. 1B**). Consistent with this prediction, mutation of K653 to Ala greatly reduced the affinity of p85α-cSH2 for PI(3,5)P_2 (**Fig. S1D** and **Table S1**) and abrogated its selectivity for PI(3,5)P_2 over PI(4,5)P_2 (**Fig. S1E**), verifying its crucial role in PI(3,5)P_2 binding. In contrast, mutation of a conserved cationic residue (R649) in the pY-binding pocket to Ala had no effect on PI(3,5)P_2 association (**Fig. S1D** and **Table S1**). When assayed by fluorescence anisotropy K653A had WT-like affinity for the cognate pY-containing peptide of p85α-cSH2 whereas R649A had lower affinity than WT by three orders of magnitude (**Fig. S1F**), showing that p85α-cSH2 has non-overlapping binding sites for PI(3,5)P_2 and pY. Collectively, these studies establish p85α-cSH2 as a *bona fide* PI(3,5)P_2-binding domain that can be used as a template for PI(3,5)P_2-specific sensor development.

Development of a PI(3,5)P_2-specific ratiometric from p85α-cSH2

We recently developed a ratiometric fluorescence sensor-based *in situ* quantitative lipid imaging technology (**Fig. 1C**), which has been successfully applied to the spatiotemporally resolved quantification of diverse cellular lipids, including PI(4,5)P_2, PIP_3, PI(3,4)P_2, phosphatidylserine, and cholesterol, in live cells (Liu et al., 2017; Liu et al., 2014; Liu et al., 2018; Yoon et al., 2011). Since it has been estimated that the cellular concentration of PI(3,5)P_2 is extremely low (Hasegawa et al., 2017; Rivero-Ríos and Weisman, 2022), an effective PI(3,5)P_2 sensor must have high PI(3,5)P_2 selectivity over more abundant PtdInsP species, PI(4,5)P_2 in particular, and a linear

response range at low PI(3,5)P_2 levels. To meet these stringent requirements, we generated a PI(3,5)P_2-specific ratiometric sensor by extensive protein engineering of the p85α-cSH2, followed by its chemical conjugation with a solvatochromic fluorophore, WCB (Sharma et al., 2020) (**Fig. 1 C, D** and **Fig. S2A**). Briefly, multiple mutations were preformed on p85α-cSH2 to eliminate its binding affinity for pY and other PtdInsPs and to introduce a single Cys on the membrane binding surface for fluorophore conjugation (see **Fig. S2A** for detailed procedures). The resulting sensor, WCB-*e*p85α-cSH2 (i.e., WCB-p85α-cSH2-R649A/C656R/Y685C), showed a large hypsochromic shift (i.e., emission maximum shifted from 490 to 430 nm) upon lipid vesicle binding, with exceptional specificity for PI(3,5)P_2 (**Fig. 1E**). Unlike p85α-cSH2 that showed significant binding to PI(4,5)P_2 (see **Fig 1A**), the engineered ratiometric sensor WCB-*e*p85α-cSH2 showed high affinity for only PI(3,5)P_2-containing vesicles (**Fig. 1E**). No other PtdInsP, including PI(4,5)P_2, enhanced the membrane affinity of *e*p85α-cSH2 over phosphatidylserine-containing vesicles (**Fig. 1E**). Also, p85α-cSH2 exhibited a sharp concentration-dependent increase in fluorescence intensity when bound to PI(3,5)P_2-containing vesicles (**Fig. 1F**). However, it showed a minimal response to changes in PI(4,5)P_2 concentration under the same conditions (**Fig. S2D**). The ratiometric PI(3,5)P_2 binding isotherm showed that WCB-*e*p85α-cSH2 has a robust response range of 0-1 mol% of PI(3,5)P_2 with a half-maximal value at 0.20 ± 0.05 mol% of PI(3,5)P_2 (**Fig. 1G**). It also exhibited low affinity for the cognate pY motif of p85α-cSH2 (**Fig. S1F**). Collectively, WCB-*e*p85α-cSH2 meets all requirements for a cellular ratiometric sensor of PI(3,5)P_2 and is hence well suited for robust, sensitive, and specific ratiometric quantification of cellular PI(3,5)P_2.

Spatiotemporally resolved quantification of cellular PI(3,5)P_2

To test the cellular specificity and efficiency of WCB-*e*p85α-cSH2, we first microinjected it into unstimulated HeLa and HEK293 cells, respectively. Microinjected WCB-*e*p85α-cSH2 only detects PI(3,5)P_2 in the cytoplasmic leaflets of organelle membranes because our ratiometric sensors cannot cross the lipid bilayer (Liu et al., 2017; Liu et al., 2014; Liu et al., 2018; Yoon et al., 2011). As shown in **Fig. 2A**, microinjected WCB-*e*p85α-cSH2 displayed a punctate intracellular distribution. Colocalization analysis with various organelle markers showed that WCB-*e*p85α-cSH2 was primarily localized at lysosomes and also significantly at late endosomes (**Fig. S3A**). No statistically significant localization was detected at early endosomes and, more importantly, PM (**Fig. S3A**). It has been reported that the PM contains the highest concentration of PI(4,5)P_2

(i.e., 1 mol%) (Liu et al., 2014; Yoon et al., 2011) and also significant levels of PI(4)P (Hammond et al., 2012) and PI(5)P (Hasegawa et al., 2017). Thus, the complete lack of sensor signal at the PM demonstrates that WCB-*e*p85α-cSH2 does not respond to PI(4,5)P_2 and other PtdInsPs. Ratiometric quantification of cross-sectional images (n = 35) illustrated the spatial distribution of PI(3,5)P_2 at the cytoplasmic leaflets of lysosomes and late endosomes at a given time (**Fig. 2B**). The spatially averaged PI(3,5)P_2 concentration was 0.15 ± 0.03 mol%. This steady-state PI(3,5)P_2 concentration is significantly lower than that reported for PI(4,5)P_2 (Liu et al., 2014; Yoon et al., 2011) and comparable to those reported for PIP_3 and PI(3,4)P_2 (Liu et al., 2018).

To validate our PI(3,5)P_2 quantification results, we measured the effects of suppressing the activity of various lipid kinases and phosphatases on the PI(3,5)P_2 level in HEK293 cells (**Fig. 2C**). First, we inhibited PIKfyve, which converts PI(3)P into PI(3,5)P_2, by either Apilimod or YM201636. The treatment, which enlarged endosomes (data not shown) as reported previously (Hasegawa et al., 2017; Rivero-Ríos and Weisman, 2022), reduced the concentration of PI(3,5)P_2 to undetectable levels (**Fig. 2D** and **Fig. S3, B and C**), verifying that WCB-*e*p85α-cSH2 specifically recognizes cellular PI(3,5)P_2. siRNA-mediated suppression of PIKfyve yielded the same results (**Fig. 2D, Fig. S3D, and Fig S4A**). We also measured the effects of inhibiting PI(3)P-producing enzymes, PI3KC2α, PI3KC2β, Vps34, and INPP4B, on PI(3,5)P_2 levels. When Vps34 was pharmacologically inhibited by SAR405 or genetically suppressed by siRNA, the spatially averaged PI(3,5)P_2 concentration at late endosomes and lysosomes was decreased to 0.05 mol% (**Fig. 2D, Fig. S3, E and F,** and **Fig S4B**), suggesting that Vps34 is a main supplier of PI(3)P molecules that are converted to PI(3,5)P_2 at steady-state. Interestingly, siRNA-mediated suppression of PI3KC2β expression also significantly reduced PI(3,5)P_2 levels (**Fig. 2D, Fig. S3G,** and **Fig S4C**), suggesting its involvement in the pathway. siRNA-mediated suppression of INPP4B and PI3KC2α displayed much smaller effects on PI(3,5)P_2 levels in HEK293 cells than that of Vps34 and PI3KC2β (**Fig. 2D, Fig. S3**, **H and I, and Fig. S4D, S4E**).

Growth factor stimulation produces a special pool of PI(3,5)P_2 via PI3KC2β

It has been reported that PI(3)P is produced by Class II PI3K in response to growth factor stimulation (Arcaro et al., 2000; Falasca et al., 2007). Since growth factor-generated PI(3)P can be also converted into PI(3,5)P_2, we quantified PI(3,5)P_2 following stimulation of HEK293 cells with growth factors. When HEK293 cells were treated with platelet-derived growth factor (PDGF), the

spatially averaged PI(3,5)P_2 concentration was increased from 0.15 to 0.23 mol% after 15 min, i.e., by >50% (**Fig. 2E**), indicating that additional PI(3,5)P_2 molecules were generated upon PDGF stimulation. Although the average value was 0.23 mol%, the local PI(3,5)P_2 concentration on individual late endosome/lysosomes varied widely, with some punctae containing up to 0.8 mol% PI(3,5)P_2 (**Fig. 2E)**. Again, pharmacological inhibition or siRNA-mediated suppression of PIKfyve abrogated PI(3,5)P_2 formation (**Fig. 2F**). Also, pharmacological inhibition or knockdown of Vps34 and PI3KC2β knockdown greatly reduced the level of PGFD-induced PI(3,5)P_2, whereas PI3KC2α and INPP4B knockdown had minimal effects (**Fig. 2F**). Importantly, although suppression of both Vps34 and PI3KC2β greatly reduced overall PI(3,5)P_2 levels before and after PDGF stimulation, only PI3KC2β-depleted HEK293 cells showed no increase in PI(3,5)P_2 upon PDGF stimulation (**Fig. 2, D, F**). These results suggest that there are at least two distinct pools of cellular PI(3,5)P_2, a steady-state form and a PDGF-induced form and that Class II PI3KC2β may play an important role in producing the latter.

To test the presence of separate steady-state and induced PI(3,5)P_2 pools, we quantified PI(3,5)P_2 in HEK293 cells after PDGF stimulation in a spatiotemporally resolved manner. From its basal level of 0.15 mol%, PI(3,5)P_2 reached 0.23 mol% at 12 min post-PDGF stimulation, then declined to basal levels after 20 min (**Fig. 2G**). Importantly, gene ablation (**Fig. 2G** and **Fig S4C**) or knockdown (**Fig. S5A** and **Fig S4C**) of the PI3KC2β not only lowered the basal PI(3,5)P_2 level but also completely eliminated the PDGF-stimulated PI(3,5)P_2 increase. Furthermore, PDGF-induced PI(3,5)P_2 production was fully restored when PI3KC2β WT was re-introduced into PI3KC2β-null HEK293 cells (**Fig. 2G** and **Fig S4C**), confirming the essential role of PI3KC2β in this process. In contrast to PI3KC2β suppression, pharmacological inhibition or knockdown of Vps34 lowered the basal level of PI(3,5)P_2 to 0.04 mol% without affecting the PDGF-induced PI(3,5)P_2 increase (**Fig. S5A**). Moreover, knockdown of PI3KC2α or INPP4B had only small effects on the basal PI(3,5)P_2 level and little to no effect on PDGF-induced PI(3,5)P_2 synthesis (**Fig. S5A**). Lastly, pharmacological inhibition or knockdown of PIKfyve, the enzyme that converts PI(3)P to PI(3,5)P_2, completely abolished PI(3,5)P_2 throughout the time course of PDGF stimulation, confirming that PDGF-induced PI(3,5)P_2 derives from PI(3)P (**Fig. S5A**).

These observations were not limited to PDGF activation of HEK293 cells as similar results were obtained after stimulation of different cells with diverse growth factors (**Fig. S5B**). For example, stimulation of HEK293 cells with epidermal growth factor (EGF) and insulin-like growth

factor1 (IGF1), respectively, resulted in similar spatiotemporal changes in PI(3,5)P_2. Activation of NIH 3T3 cells by PDGF and HeLa cells by IGF1, respectively, also yielded similar results. Furthermore, PI3KC2β knockdown abrogated EGF-induced PI(3,5)P_2 formation in HEK293 cells, IGF1-induced PI(3,5)P_2 formation in HeLa cells, and PDGF-induced PI(3,5)P_2 production in NIH 3T3 cells (**Fig. S5B**). Taken together, these results unravel a hitherto unknown growth factor-induced production for PI(3,5)P_2, which is primarily driven by PI3KC2β.

Growth factor stimulation produces a special pool of PI(3)P via PI3KC2β

To determine how PI3KC2β contributes to the PDGF-induced PI(3,5)P_2 increase, we quantified the cellular PI(3)P level. For this purpose, we generated a ratiometric PI(3)P sensor, DAN-*e*EEA1, from the PI(3)P-specific FYVE domain of EEA1 (**Fig. S6A**). As was the case with WCB-*e*p85α-cSH2, DAN-*e*EEA1 met all requirements for a specific PI(3)P ratiometric sensor: i.e., high PI(3)P specificity, high sensitivity, and robust linear response to PI(3)P at physiological levels (i.e., 0-1.5 mol%) (**Fig. S6, B** and **C**). Tandem FYVE domains have been commonly used for fluorescence protein-based genetically encoded PI(3)P probes because a single FYVE domain does not have high enough membrane affinity (Gillooly et al., 2000). In the case of DAN-*e*EEA1, however, a single FYVE domain was sufficient for high affinity binding to PI(3)P at physiological levels because the chemically conjugated amphiphilic DAN group (**Fig. S6A**) enhances the membrane affinity of a lipid binding domain (Yoon et al., 2011). We microinjected DAN-*e*EEA1 into HEK293 cells, stimulated them with PDGF, and performed *in situ* quantifications of PI(3)P at early endosomes, where a large majority of PI(3)P is known to reside (Schink et al., 2013). The spatially averaged PI(3)P concentration was 0.41 ± 0.04 mol% in unstimulated cells (**Fig. S6D**), which rose to 0.52 ± 0.04 mol% at 6 min post-PDGF stimulation and gradually declined to the basal level (**Fig. 2H**). Pharmacological inhibition or knockdown of Vps34 greatly reduced the basal level of PI(3)P to 0.2 mol% but did not eliminate the PDGF-induced PI(3)P spike (**Fig. 2H**). These data indicate that Vps34 is responsible primarily for producing the steady-state pool of PI(3)P but it is dispensable for the generation of PDGF-induced PI(3)P. Importantly, gene ablation (**Fig. 2H**) or suppression (**Fig. S6E**) of PI3KC2β not only reduced the basal PI(3)P level but also eliminated the PDGF-induced PI(3)P peak, indicating that the latter derives primarily from phosphorylation of PI by PI3KC2β. A combination of Vps34 inhibition and PI3KC2β knockdown essentially abolished all PI(3)P signals (**Fig. S6E**). siRNA knockdown of PI3KC2α and INPP4B

had little to no effect on the PDGF-induced PI(3)P spike while modestly reducing the basal PI(3)P level (**Fig. S6E**). Lastly, siRNA knockdown of PIKfyve enhanced the total PI(3)P concentration, as expected from its role in converting PI(3)P to PI(3,5)P_2, but did not affect the kinetics of induced PI(3)P formation (**Fig. S6E**).

PI(3,5)P_2 contributes to termination of growth factor-induced Class I PI3K activity.

The mechanism of activation of Class I PI3K has been studied in detail (Zhang et al., 2011). In the resting state, the catalytic p110 subunit is autoinhibited by the regulatory p85 subunit. Upon cell stimulation two SH2 domains in p85 bind to pY's in an activating protein, such as a receptor tyrosine kinase or an adaptor protein, which relieves p110 from inhibitory tethering by p85 (Zhang et al., 2011). Although it is generally thought that Class I PI3K signaling is terminated through the action of lipid phosphatases, including PTEN and INPP4B (Bilanges et al., 2019; Fruman et al., 2017), which remove PIP_3 and PI(3,4)P_2, respectively, little is known about the mechanism that inactivates Class I PI3K itself post-stimulation. We recently reported (Liu et al., 2018) that the growth factor-induced formation of PIP_3, which directly reflects the cellular Class I PI3K activity, was limited to the PM and that the PIP_3 concentration at the PM increases and decreases rapidly (i.e., within 10 min post stimulation) (see also **Fig. 3A**). Genetic ablation of PTEN, which converts PIP_3 to PI(4,5)P_2 and is thus generally thought to counteract the Class I PI3K, had little effect on the kinetics of PIP_3 decrease after PDGF stimulation although it enhanced the amplitude of the PIP_3 peak (**Fig. S7A**). Furthermore, pharmacological inhibition of SHIP2, which is mainly responsible for conversion of PIP_3 to PI(3,4)P_2 in PDGF-stimulated cells (Liu et al., 2018), only slightly slowed down the PIP_3 decrease (**Fig. S7A**). These results suggest the presence of a hitherto unknown mechanism for termination of growth factor-stimulated Class I PI3K activity.

Our finding that PI(3,5)P_2 directly binds to p85-cSH2 with high affinity and specificity implies that PI(3,5)P_2 might be involved in regulating PI3K activity. To test this notion, we performed *in situ* quantification of PDGF-induced PIP_3 in the PM of HEK293 cells using our ratiometric PIP_3 sensor (Liu et al., 2018) while modulating the activity of lipid kinases and phosphatases involved in PI(3,5)P_2 metabolism. Consistent with our previous results (Liu et al., 2018), PDGF stimulation raised the PIP_3 concentration from 0.15 to 0.50 mol% within 4 min, which was followed by a rapid decrease of PIP_3 to basal levels within 10 min (**Fig. 3A**). Interestingly, this kinetics of PIP_3 decrease was synchronized with the kinetics of PI(3,5)P_2 formation (see **Fig. 2G**): i.e., decrease of

PIP_3 coincided with an increase of $PI(3,5)P_2$. Furthermore, pharmacological inhibition or knockdown of PIKFyve, which essentially removed all cellular $PI(3,5)P_2$ (see **Fig. S5A**), greatly slowed the PIP_3 decline phase (**Fig. 3A**). Even after 20 min, the PIP_3 level remained at about 0.3 mol%, which was about 60% of its peak concentration, indicating that Class I PI3K activation was sustained to a large extent. This effect was $PI(3,5)P_2$-specific as other treatments with minimal effects on $PI(3,5)P_2$ levels (i.e., PI3KC2α and INPP4B knockdown; see **Fig. 2E** and **Fig. S5A**) had no effect on kinetics of PIP_3 rise or decline (**Fig. S7B**). Furthermore, pharmacological inhibition or knockdown of Vps34, which reduced basal PI(3)P and $PI(3,5)P_2$, but not the PDGF-induced rise in PI(3)P and $PI(3,5)P_2$ (see **Fig. S5A**), had no effect on PIP_3 kinetics (**Fig. S7B**). These results indicate that the PDGF-induced pool of $PI(3,5)P_2$ inhibits Class I PI3K activity. Importantly, this idea was corroborated by the finding that PIP_3 levels reached a peak and did not appreciably decline for >30 min in PI3KC2β-suppressed (**Fig. 3A**) or PI3KC2β-null HEK293 cells (**Fig. 3B**). Furthermore, re-introduction of PI3KC2β WT to the PI3KC2β-null HEK293 cells fully restored the original PIP_3 kinetics of WT HEK293 cells (**Fig. 3B**). Similarly, PI3KC2β knockout slowed the PIP_3 decrease in IGF1-stimulated HEK293 cells (**Fig. S7C**) and PIKFyve knockdown slowed the PIP_3 decrease in EGF-stimulated HeLa cells (**Fig. S7D**), supporting the universal nature of the effect of $PI(3,5)P_2$ on Class I PI3K activity. Collectively, these findings unravel a crucial role of PI3KC2β/PIKFyve-generated $PI(3,5)P_2$ in feedback inhibition and termination of growth factor-stimulated Class I PI3K signaling activity.

To test the functional significance of PI(3,5)P-mediated feedback inhibition of Class I PI3K, we measured the cellular activity of endogenous Akt1 that is activated by PIP_3. S474 phosphorylation (pS474) of Akt1 by mTORC2 in HEK293 cells was reversed within 20 min after PDGF stimulation but remained largely unchanged after 20 min when cells were pre-treated with a PIKFyve inhibitor, YM201636 (**Fig. 3 C** and **D**). Akt1 also remained in its active phosphorylated state for an extended period of time in PI3KC2β-null HEK293 cells (**Fig. 3 C** and **D**).

$PI(3,5)P_2$ inhibits Class I PI3K by displacing it from $PI(4,5)P_2$-containing membranes.

To test if the observed inhibition of Class I PI3K by $PI(3,5)P_2$ is caused by direct $PI(3,5)P_2$-p85 interaction and to understand how $PI(3,5)P_2$ that is mainly found in endolysosomes can inhibit the action of Class I PI3K at PM, we performed both enzyme kinetic and membrane binding studies of Class I PI3Kα (equimolecular p110 α + p85α) using model membranes with defined lipid

compositions. For enzyme kinetics of PI3Kα, we employed a recently developed *in vitro* activity assay that allows direct real-time monitoring of the reaction and accurate quantitative analysis of kinetic parameters (Sun et al., 2020). The assay system consists of POPC/POPS/PI(4,5)P_2 (77:20:3) LUVs, a ratiometric PI(4,5)P_2 sensor, PI3Kα, a pY-containing peptide derived from PDGFβ (pY2), and ATP. The reaction is typically triggered by adding ATP to the reaction mixture containing all other elements and the reaction progress is directly and continuously monitored spectrofluorometrically by following the time course of the ratio of fluorescence emission intensity at two maximal wavelengths before and after the hypsochromic shift, respectively. We reasoned that for PI(3,5)P_2, which is primarily synthesized within the endolysosomal system, to inhibit PI3Kα at the PM, it should be able to inhibit the action of PI3Kα in a *trans*-vesicular mode (**Fig. 4A**). **Fig. 4B** shows the typical kinetic curves of PI(4,5)P_2 phosphorylation by PI3Kα, which could be analyzed using a simple Michaelis-Menten kinetic equation (Sun et al., 2020). We previously reported that PI3Kβ is competitively inhibited by its reaction product, PIP_3 in a *cis* mode (Sun et al., 2020). Consistent with this finding, PI3Kα was also inhibited by pre-added PIP_3 in the PI(4,5)P_2-containing vesicles (i.e., POPC/POPS/PI(4,5)P_2/PIP_3 (77-*x*/20/3/*x*; *x* = 0-3 mole%)) in a concentration-dependent manner (**Fig. S8A**). Under the same conditions, PI(3,5)P_2 had no effect on PI3Kα activity: i.e., the initial rate was unaltered when the PI(3,5)P_2 composition was varied in POPC/POPS/PI(4,5)P_2/PI(3,5)P_2 (77-*x*/20/3/*x*; *x* = 0-3 mole%) LUVs (**Fig. S8B**). This indicates that PI(3,5)P_2 neither competes with PI(4,5)P_2 for the catalytic site in PI3Kα nor causes allosteric inhibition of PI3Kα in a *cis* mode. Importantly, however, when separate POPC/POPS/PI(3,5)P_2 (77:20:3) LUVs were added to the reaction mixture containing POPC/POPS/PI(4,5)P_2 (77:20:3) LUVs, the rate of reaction was significantly reduced (**Fig. 4B**). Systematic inhibition analysis using equimolar mixtures of POPC/POPS/PI(4,5)P_2 (77:20:3) and POPC/POPS/PI(3,5)P_2 (80-*x*/20/*x*; *x* = 0-3 mole%) LUVs showed that PI(3,5)P_2 can potently inhibit PI3Kα in a concentration-dependent manner (**Fig. 4, B** and **D**) in a *trans* mode; i.e. by displacing it from PI(4,5)P_2-containing vesicles. Equimolar PI(3,5)P_2 in the trans LUVs caused ～70% inhibition of PI3Kα. When LUVs containing other PtdInsPs (e.g., POPC/POPS/PIP_3 (77:20:3) or POPC/POPS/PI(3)P (77:20:3)) were added to the reaction mixture, none caused appreciable inhibition of PI3Kα in a *trans* mode (**Fig. S8, C** and **D**). This demonstrates the specificity of *trans*-vesicular PI(3,5)P_2 inhibition. To verify that the observed inhibition is specifically mediated by p85-cSH2-PI(3,5)P_2 interactions, we employed a PI3Kα mutant (p110α + p85α-K653A) whose p85α subunit harbors the K653A

mutation that specifically reduces PI(3,5)P_2 binding of the p85-cSH2 (see **Fig. S1D** and **Table S1**). This variant was as active as PI3Kα WT toward POPC/POPS/PI(4,5)P_2 (77:20:3) LUVs but was not inhibited by externally added equimolar POPC/POPS/PI(3,5)P_2 (77-*x*/20/*x*; *x* = 0-3 mole%) LUVs **(Fig. 4, C** and **D)**. These *in vitro* kinetic studies show that PI(3,5)P_2 can potently and specifically inhibit Class I PI3Kα acting on remote PI(4,5)P_2-containing membranes presumably by displacing the p110α-p85α heterodimer from the membranes.

To check whether or not PI(3,5)P_2 can physically displace the p110α-p85α heterodimer from PI(4,5)P_2-containing membranes during the enzyme catalysis, we performed confocal microscopic imaging experiments under the same conditions. Specifically, we monitored the binding and unbinding of enhanced green fluorescence protein (EGFP)-tagged PI3Kα (i.e., EGFP-p110α + p85α) to and from giant unilamellar vesicles (GUVs) containing POPC/POPS/PI(4,5)P_2/1,2-dioleoyl-sn-glycero-3-phosphoethanolamine-N-(lissamine rhodamine B sulfonyl) (Rh-PE) (67:20:3:10) in the presence of externally added PI(3,5)P_2-containing GUVs. Rh-PE was used as a GUV marker. It was reported that pY2 induces conformational changes and membrane binding of Class I PI3K by simulating the effect of binding of p85 to an activated growth factor receptor or its adaptor proteins (Zhang et al., 2011). Upon adding pY2 to the mixture containing EGFP-PI3Kα and POPC/POPS/PI(4,5)P_2/Rh-PE GUVs, a significant increase in EGFP fluorescence intensity on these GUV surfaces was detected (**Fig. 4E**), indicating that pY2 triggered binding of EGFP-PI3Kα to PI(4,5)P_2-containing GUVs. We then added POPC/POPS/PI(3,5)P_2 (80-*x*/20/*x*; *x* = 0-3 mole%) GUVs to the mixture, which caused immediate and full unbinding of EGFP-PI3Kα from PI(4,5)P_2-containing GUVs as essentially all EGFP fluorescence intensity was shifted from PI(4,5)P_2-containing to PI(3,5)P_2-containing GUVs **(Fig. 4E, F)**. The PI(3,5)P_2 concentration dependency of EGFP-PI3Kα dissociation from PI(4,5)P_2-containing GUVs shows that even 0.5 mole% of PI(3,5)P_2 can remove >80% of EGFP-PI3Kα from GUVs containing 1 mole% PI(4,5)P_2, again demonstrating the efficiency of this PI(3,5)P_2-mediated *trans*-vesicular displacement (**Fig. 4F**). Also the PI(3,5)P_2 concentration dependency of EGFP-PI3Kα binding to PI(3,5)P_2 GUVs was essentially the mirror image of that of EGFP-PI3Kα dissociation from PI(4,5)P_2 GUVs (**Fig. 4F**). Collectively, these enzyme kinetic and membrane binding data show that PI(3,5)P_2 can inhibit the Class I PI3K activity in a *trans*-membrane mode by displacing it from the substrate (i.e., PI(4,5)P_2)-containing membranes. The high efficiency of this inhibition also supports the notion that PI(3,5)P_2 can inhibit cellular activity of Class I PI3K by the same mechanism.

PI(3,5)P_2 inhibits Class I PI3K by displacing it from the plasma membrane of mammalian cells via direct interaction.

To check if this inhibition-by-displacement mechanism also works in living cells, we performed a wide range of quantitative cellular imaging measurements while modulating the cellular PI(3,5)P_2 level. For PIKfyve inhibition, either siRNA knockdown or pharmacological inhibition was employed depending on feasibility under specific experimental conditions. First, we performed total internal reflection fluorescence microscopy (TIRFM)-based single molecule tracking of PI3Kα at the PM of p110-null mouse embryonic fibroblast (MEF) cells, whose endogenous p85α and p85β regulatory subunits were also depleted by siRNAs (**Fig. S4F**). Specifically, we exogenously expressed EGFP-p110α-p85α-WT (PI3Kα WT) and the EGFP-p110α-p85α-K653A (PI3Kα-K653A) mutant at the lowest possible levels, respectively, in these MEFs and compared their PM residence upon PDGF stimulation. In general, EGFP-PI3Kα WT rapidly appeared on and disappeared from the PM after PDGF stimulation (**Fig. S9A**). Single molecule tracking analysis showed that the average PM dwell time of EGFP-PI3Kα WT, expressed in terms of the half-life of PM dissociation, peaked (≈150 msec) at 5 min post-stimulation and declined afterwards (**Fig. 5A**). This analysis indicates that the population of PI3Kα WT at PM reached a maximum at 5 min after stimulation, which is well synchronized with the kinetics of PIP_3 formation at the PM (see **Fig. 3A**). When compared with PI3Kα WT, PI(3,5)P_2 binding-defective mutant PI3Kα-K653A exhibited much more sustained PM residence after reaching its peak (**Fig. 5A** and **Fig S9A**). Furthermore, treatment of cells with a PIKfyve inhibitor, YM201636, greatly slowed the dissociation phase and elongated the PM dwell time of PI3Kα WT (**Fig. 5A** and **Fig S9A**). Overall, these results are consistent with the notion that PI3Kα, which is recruited to the PM upon PDGF stimulation, is rapidly displaced from the PM via p85-PI(3,5)P_2 interaction after PDGF stimulation.

To monitor the spatiotemporal dynamics of PI3Kα under physiological conditions, we also determined the subcellular localization of endogenous Class I PI3K in HEK293 cells after PDGF stimulation by immunostaining using a p85-specific antibody. It has been reported that the amplitude and duration of growth factor signaling is regulated by receptor trafficking (Bergeron et al., 2016; Koseska and Bastiaens, 2020; Schoenherr et al., 2018). These reports suggested that our observed inhibition of the PI3Kα activity on PM by lysosomal PI(3,5)P_2 could occur by at least two distinct mechanisms; i.e., via direct transmembrane movement or endocytosis of PI3Kα. If

PI3Kα reaches lysosomes by direct transmembrane hopping, one would expect that endocytosis inhibition would not interfere with the kinetics of PIP_3 decline and the lysosomal localization of PI3Kα. Upon PDGF stimulation, the relative population of PI3K at PM peaked at 5 min then reached the basal level after 20 min (**Fig. 5B** and **Fig. S9B**), which is again consistent with the kinetics of PM localization and enzymic action of PI3K shown in **Fig. 5A** and **Fig. 3A**, respectively. Also, PM dissociation of PI3K was greatly inhibited by $PI(3,5)P_2$ depletion by PIKFyve knockdown (**Fig. 5B** and **Fig. S9B**). However, inhibition of endocytosis in the presence of the clathrin inhibitor Pitstop2 (von Kleist et al., 2011), which has been also reported to inhibit clathrin-independent endocytosis (Dutta et al., 2012; Willox et al., 2014), did not affect PM dissociation of PI3Kα (**Fig. 5B** and **Fig. S9B**). Furthermore, Pitstop2 treatment did not change the kinetics of PIP_3 decline (**Fig. S7A**). These results show that PDGF-stimulated PI3Kα is rapidly displaced from the PM via direct p85-$PI(3,5)P_2$ interaction, but not via endocytosis of PM-bound PI3Kα under physiological conditions. Consistently, Class I PI3K, when stained with the p85-specific antibody, showed statistically significant colocalization with LAMP1-containing lysosomes at 10 min post-stimulation (**Fig. 5C** and **Fig. S9C**). Colocalization of PI3K with lysosomal LAMP1 was synchronized with the decline in PIP_3 formation at the PM (see **Fig. 3A**) and was abrogated by siRNA knockdown of PIKfyve, but not by Pitstop2 treatment (**Fig. 5C** and **Fig. S9C**). Similar results were observed when a p110α-specific antibody was used in lieu of the anti-p85 antibody (**Fig. S10A**).

To obtain higher resolution images of $PI(3,5)P_2$-dependent lysosomal localization of PI3K during its catalysis, we also performed the expansion microscopy of PI3K in HEK293 cells, using the p85 antibody, after PDGF stimulation. Imaging data after 4-fold expansion of the specimen clearly demonstrate the lysosomal localization of PI3K after PDGF stimulation, which was again abrogated by PIKfyve inhibition (**Fig. 5D** and **Fig, S9D**). Also, the kinetics of lysosomal localization of PI3K was well synchronized with the kinetics of PIP_3 decline in the PM (see **Fig. 3A**). Collectively, our results show that both p85 and p110 subunits of PI3K are displaced from the PM and directly recruited to lysosomes in the presence of $PI(3,5)P_2$.

Our finding that Pitstop2 showed no effect on the PM localization of PI3K (see **Fig. 5B**), lysosomal localization of PI3K (**Fig. S9C**), and the kinetics of PDGF-induced PIP_3 formation at the PM (**Fig. S7A**) argues against the possibility that PI3K on PM is inhibited by lysosomal $PI(3,5)P_2$ via endocytosis of PI3K. To preclude the possibility of $PI(3,5)P_2$-facilitated endocytosis

and lysosomal translocation of PI3K, we also monitored endocytic movement of endogenous PI3K to early endosomes in HEK293 cells after PDGF stimulation by immunostaining. Specifically, we monitored the time-lapse movement of PI3K from PM to early endosomes while inhibiting endocytosis by Pitstop2 and suppressing PI(3,5)P_2 production by siRNA-mediated PIKFyve knockdown. After PDGF stimulation, PI3K did not show any detectable early endosome localization whether or not cells were pre-treated with Pitstop2 and PIKfyve siRNA, respectively (**Fig. 5E** and **Fig. S9E**). Similar results were observed when the p110α-specific antibody was used in lieu of the anti-p85 antibody (**Fig. S10B**).

Collectively, these cell imaging results obtained by different imaging methods under various conditions strongly support the notion that PI(3,5)P_2 present in lysosomes/late endosomes inhibits the action of Class I PI3K at the PM by specifically binding to p85-cSH2 and thereby directly removing PI3K from its primary site of its action.

Hot-spot mutations in p85 cause sustained Class I PI3K activation by inhibiting p85-PI(3,5)P_2 binding.

Somatic mutations of p110α and p85α subunits have been found in various cancer cells and some 'hot-spot' mutations are known to drive cancer cell transformation (Bilanges et al., 2019; Fruman et al., 2017; Zhang et al., 2021). Although much is known about the effects of hot-spot mutations in p110α, less is known about those of hot-spot mutations in p85α. The most common hot-spot p85α mutations are located in the nSH2 (e.g., G376R and K379E) and iSH2 domains (e.g., R461A and N564D) but some mutations (e.g., R642L) are also found in the PI(3,5)P_2-binding site of the cSH2 domain (Bilanges et al., 2019; Fruman et al., 2017; Marshall et al., 2019). These mutations are generally known to enhance PI3K activity by relieving autoinhibition of p110 by p85 (Bilanges et al., 2019; Fruman et al., 2017; Marshall et al., 2019). As described earlier, although p85-cSH2 has higher PI(3,5)P_2 specificity than p85-nSH2, the latter can also tightly bind PI(3,5)P_2 (see **Table S1**). We thus hypothesized that hot-spot mutations in p85-nSH2 could also affect the p85-PI(3,5)P_2 interaction directly or indirectly. To test this notion, we measured the effects of the common oncogenic p85α mutations on the kinetics of PIP_3 formation by reintroducing p85α mutants to HEK293 cells, whose endogenous p85 was depleted by siRNA (**Fig. S4G**). siRNA-mediated suppression of endogenous p85α and p85β in HEK293 cells greatly slowed the decline phase of the PIP_3 kinetics, which was fully restored when p85α WT was re-introduced (**Fig. 6A** and **Fig.**

S4G). In contrast, re-introduction of p85α-K653A with compromised PI(3,5)P_2 binding (see **Table S1**) could not restore the fast PIP_3 decline (**Fig. 6A** and **Fig. S4G**), verifying that the p85α-PI(3,5)P_2 interaction is primarily responsible for PI3K inactivation. Importantly, reintroduction of all common oncogenic p85α mutants into p85-deficient cells consistently led to sustained PIP_3-production (**Fig. 6B** and **Fig. S4H**) although the magnitude of their effects varied to some degree. Between the two iSH2 domain mutants, N564D behaved like other nSH2 and cSH2 mutants whereas R461A had only a minor effect on the PIP_3 kinetics (**Fig. 6B**). This is consistent with the fact that the iSH2 region is not directly involved in PI(3,5)P_2 binding but can indirectly affect PI(3,5)P_2 binding of nSH2 and cSH2 domains. We also measured the *in vitro* activity of the selected p85α mutants (i.e., p110α WT + p85α-mutant (G376R, K379E, and R642L)) toward POPC/POPS/PI(4,5)P_2 (77:20:3) LUVs in the presence of separate POPC/POPS/PI(3,5)P_2 (80-x/20/x; x = 0-3 mole%) LUVs. Akin to the specific PI(3,5)P_2-binding site mutant (K653A), these oncogenic mutants were not inhibited by PI(3,5)P_2-containing vesicles (**Fig. 4D** and **Fig. S11, A-C**). Collectively, these results show that many hot-spot mutations in the nSH2 and cSH2 domains of the p85α subunit of Class I PI3K drastically suppress p85α-PI(3,5)P_2 binding and consequent feedback inhibition of Class I PI3K, thereby promoting sustained PI3K signaling activity.

DISCUSSION

Due to their involvement in various human diseases, most notably cancer, Class I PI3Ks have been a focus of extensive studies (Bilanges et al., 2019; Fruman et al., 2017). Although much is known about the structure, function, and cellular activation mechanisms of Class I PI3Ks (Bilanges et al., 2019; Fruman et al., 2017), much less is known about how the activated Class I PI3Ks are turned off after stimulation. Our spatiotemporally resolved quantification of PIP_3 has shown that growth factor-induced formation of PIP_3 at the PM of common mammalian cell lines, including HEK293, NIH3T3, and HeLa cells, is rapidly (i.e., within 15 min) declined after reaching a peak at about 5 min post stimulation, resulting in only a short burst of PIP_3 (Liu et al., 2018). It is generally thought that PI3K-mediated PIP_3 formation is counterbalanced by lipid phosphatases, most notably PTEN and SHIP2/INPP4, which convert PIP_3 to PI(4,5)P_2 and PI(3,4)$_2$/PI(3)P, respectively. Genetic ablation of PTEN and suppression of SHIP2 and INPP4B (Liu et al., 2018) do not substantially alter the kinetics of PIP_3 disappearance, indicating that the rapid removal of PIP_3 at PM is not driven by enzymatic transformation of PIP_3 by lipid phosphatases. These results also suggest that

lipid phosphatases alone cannot attenuate the PIP_3 signal at PM as long as Class I PI3K remains active. Since the activation of Class I PI3K is not known to be driven by post-translational modification (Bilanges et al., 2019; Fruman et al., 2017), it cannot be reversed by counterbalancing modification. One can speculate alternative mechanisms, such as degradation of Class I PI3K and endocytic sequestration of Class I PI3K. However, conclusive evidence for these mechanisms has not been reported. The present study shows that hitherto unknown $PI(3,5)P_2$-mediated feedback inhibition plays a pivotal role in reversing activation of Class I PI3K induced by PDGF and other growth factors. Key evidence for the new mechanism is provided by our spatiotemporally resolved *in situ* quantification of two other 3'-phosphoinositides, PI(3)P and $PI(3,5)P_2$, which was made possible by newly developed ratiometric sensors for these lipids. In particular, development of the elusive $PI(3,5)P_2$-specific sensor represents a major technical breakthrough that has enabled us to gain new mechanistic insight into $PI(3,5)P_2$-mediated cell regulation. Our imaging data under various conditions clearly show that growth factor stimulation leads to Class II PI3KC2β-mediated formation of PI(3)P on endosomes, which is converted into a special pool of $PI(3,5)P_2$ by PIKFyve on late endosomes/lysosomes (**Fig. 6C**). This induced pool of $PI(3,5)P_2$, but not a steady-state pool of $PI(3,5)P_2$, turns off the PIP_3-producing activity of Class I PI3K by displacing it from the $PI(4,5)P_2$-abundant PM through specific interaction with the two SH2 domains in the p85 subunit (**Fig. 6C**). This inhibition-by-displacement mechanism is supported by multiple lines of biophysical, enzyme kinetics, and cell imaging data.

Results from the in vitro enzyme activity assay and imaging measurements show that $PI(3,5)P_2$ can efficiently and potently inhibit PI3Kα acting on $PI(4,5)P_2$-containing vesicles in a *trans*-vesicular mode. The enzyme activity of PI3Kα on $PI(4,5)P_2$-containing vesicles is reduced by 70% in the presence of separate vesicles containing equimolar $PI(3,5)P_2$. Confocal imaging data show that $PI(3,5)P_2$ in separate vesicles can efficiently displace activated PI3Kα bound to $PI(4,5)P_2$-containing vesicles under the same conditions. Our previous studies have shown that the concentration of $PI(4,5)P_2$ at the PM fluctuates between 0.6 and 1.0 mol% during PDGF-induced PI3K activation in various mammalian cells (Liu et al., 2014; Liu et al., 2018). The present study shows that although spatially averaged $PI(3,5)P_2$ concentration rises from 0.15 to 0.25 mol% after PDGF stimulation, the local $PI(3,5)P_2$ concentration varies widely, with some endolysosomal spots exhibiting up to 0.8 mol% of $PI(3,5)P_2$ (see **Fig. 2E**). Our immunostaining data (**Fig. S9B**) suggest that only a small fraction of endogenous Class I PI3K is recruited to the PM upon PDGF

stimulation. Thus, quantitative inhibition of PM-bound Class I PI3K by endosomal/lysosomal PI(3,5)P_2 should be locally feasible and efficient under physiological conditions.

This notion is fully supported by our quantitative cell imaging. Both single molecule tracking of exogenously expressed PI3Kα and immunostaining of endogenous PI3K show that Class I PI3K is recruited to the PM upon PDGF stimulation but rapidly displaced from the PM via PI(3,5)P_2-p85 interaction. The kinetics of PI(3,5)P_2-mediated PM displacement of PI3K is well synchronized with the kinetics of PIP_3 decline at the PM, indicating that the PI(3,5)P_2-mediated PM displacement of PI3K is primarily responsible for the rapidly decreasing PI3K activity at the PM. Importantly, both conventional and super-resolution expansion microscopy-based imaging demonstrate that the PI(3,5)P_2-p85 interaction moves a majority of PI3K from PM to lysosomes, the kinetics of which is again well synchronized with the kinetics of PIP_3 clearance at the PM. The lysosomal movement of PI3K may be facilitated by the growth factor-induced dispersion of lysosomes to the cell periphery (Korolchuk et al., 2011).

It is well documented that the amplitude and duration of growth factor signaling is regulated by receptor trafficking (Bergeron et al., 2016; Koseska and Bastiaens, 2020; Schoenherr et al., 2018). It was recently reported that PI3Kα is endocytosed upon growth factor stimulation and actively produces PIP_3 in endomembranes (Thapa et al., 2020). We (Liu et al., 2018) and others (Chen et al., 2021) have reported endocytosis-mediated delivery of PI(3,4)P_2 to endomembranes for downstream signaling pathways; however, our spatiotemporally resolved quantitative imaging detected neither the substrate (i.e., PI(4,5)P_2) nor the product (i.e., PIP_3) of Class I PI3K on endomembranes, early endosomes in particular, after PDGF stimulation (Liu et al., 2018). Further studies are needed to fully understand the origin of this discrepancy but our results clearly show that PI(3,5)P_2 on endomembranes moves PI3K from the PM to lysosomes through direct interaction with the SH2 domains of p85, but not through modulating endocytosis of PI3K. Also, the fact that PIKfyve inhibition, which removes lysosomal PI(3,5)P_2 and causes sustained PIP_3 formation at the PM, has no effect on early endosomal localization of PI3K precludes the possibility PI(3,5)P_2 exerts its inhibitory effect on Class I PI3K by modulating its endocytosis. In fact, although PI(3,5)P_2 has been reported to be involved in endocytic recycling to the PM, its involvement in receptor endocytosis to early endosomes has not been reported to date (Rivero-Ríos and Weisman, 2022).

Extensive somatic mutations of Class I PI3Ks have been identified in various human cancer (Bilanges et al., 2019; Fruman et al., 2017). In particular, *PIK3CA*, which encodes the p110α catalytic subunit of PI3Kα, is the most frequently mutated gene in breast cancer (Bilanges et al., 2019; Fruman et al., 2017). Common hot-spot mutations in p110α (e.g., E542K, E545K and H1047R) activate PI3K by perturbing inhibitory intramolecular interaction between p85 and p110α and/or enhancing membrane affinity of p110α (Bilanges et al., 2019; Fruman et al., 2017; Zhang et al., 2021). Somatic mutations of *PIK3R1*, which encodes p85α, is less common than *PIK3CA* mutations, but they are found at high frequency in several cancer types, including endometrial, colorectal, and prostate cancer and glioblastoma (Marshall et al., 2019). The most common p85α point mutations are located within the nSH2 domain and iSH2 domain (Marshall et al., 2019). It has been speculated that hot-spot mutations in the nSH2 domain of p85α, such as G376R and K379E, may cause gain-of-function effects by weakening the inhibitory p110-p85α interaction (Marshall et al., 2019). Our results show that these mutations as well as mutations in the cSH2 suppress p85-PI(3,5)P_2 interaction and thereby block the feedback inhibition of Class I PI3K by PI(3,5)P_2, causing sustained activation of Class I PI3K. These results not only provide further credence to the pathophysiological significance of newly discovered PI(3,5)P_2-mediated feedback inhibition of Class I PI3K activity but also suggest a new therapeutic possibility of treating cancer patients with p85α mutations by modulating the cellular level of a specific pool of PI(3,5)P_2.

LIMITATIONS OF THE STUDY

Although the present study provides new insight into the mechanism of growth factor-mediated Class I PI3K regulation, questions still remain as to how Class II PI3KC2β maybe activated by growth factors and how growth factor-induced PI(3,5)P_2 can specifically and potently inhibit Class I PI3K activity while the steady-state PI(3,5)P_2 cannot. Earlier studies reported that Class II PI3KC2, which has PI(4,5)P_2-binding PX and C2 domains (Stahelin et al., 2006), can be recruited to the PM and activated via phosphorylation upon growth factor stimulation (Arcaro et al., 2000; Falasca et al., 2007; Wheeler and Domin, 2001); however, further studies are necessary to fully elucidate the spatial and temporal mechanism by which PI3KC2β is activated by growth factors. The mechanism identified here may further synergize with the recently established role of PI3KC2β in the local repression of mTORC1 signaling, a major downstream effector of the Class

I PI3K pathway, under growth factor-starved conditions (Marat et al., 2017) to keep the activity of the PI3K-Akt-mTOR signaling axis under control.

The extremely low cellular abundance of PI(3,5)P_2 makes it technically challenging to determine the structural differences of basal and induced PI(3,5)P_2 by mass spectrometry, but one can speculate that they may originate from different phosphatidylinositol pools and thus have different acyl chain compositions. Lipid-protein interaction across two separate membranes via membrane contact sites has been well documented (Prinz et al., 2020). Although signaling via a membrane contact site between PM and endolysosomes has not been reported, lysosome-PM fusion has been well established in the secretory pathway (Tancini et al., 2020). It is thus possible that the growth factor-induced PI(3,5)P_2 is more closely localized to the PM than the basal PI(3,5)P_2. Although the current spatial resolution of our ratiometric lipid imaging does not allow clear distinction of potentially different subcellular distribution of basal and induced PI(3,5)P_2, further improvement of the lipid quantification technology through development of new fluorophores and imaging modalities should enable us to address this important mechanistic question in the near future.

ACKNOWLEDGEMENTS

This work was supported by grants from the National Institutes of Health (R35GM122530 to WC), (R35CA210057 to JJZ), the European Union (ERC AdG 884 281 to VH) and the Deutsche Forschungsgemeinschaft (TRR186/ A08 to VH). RG acknowledges funding support from Scialog grant #28707, sponsored jointly by Research Corporation for Science Advancement and the Walder Foundation.

AUTHOR CONTRIBUTIONS

JS carried out all lipid quantification. SS and IS performed SPR studies. AS synthesized solvatochromic fluorophores. YH contributed to initial lipid sensor development. WTL, PAG, and VH assisted in PI3KC2β work. WW and RG contributed to expansion microscopy imaging. JJZ assisted in p110 gene ablation work. WC conceived and supervised the work and wrote the paper.

DECLARATION OF INTERESTS

The authors declare no competing interests.

REFERENCES

Adler, J., and Parmryd, I. (2013). Colocalization analysis in fluorescence microscopy. Methods Mol Biol *931*, 97-109.

Arcaro, A., Zvelebil, M.J., Wallasch, C., Ullrich, A., Waterfield, M.D., and Domin, J. (2000). Class II phosphoinositide 3-kinases are downstream targets of activated polypeptide growth factor receptors. Mol Cell Biol *20*, 3817-3830.

Asano, S.M., Gao, R., Wassie, A.T., Tillberg, P.W., Chen, F., and Boyden, E.S. (2018). Expansion Microscopy: Protocols for Imaging Proteins and RNA in Cells and Tissues. Curr Protoc Cell Biol *80*, e56.

Balla, T. (2013). Phosphoinositides: tiny lipids with giant impact on cell regulation. Physiol Rev *93*, 1019-1137.

Bergeron, J.J., Di Guglielmo, G.M., Dahan, S., Dominguez, M., and Posner, B.I. (2016). Spatial and Temporal Regulation of Receptor Tyrosine Kinase Activation and Intracellular Signal Transduction. Annu Rev Biochem *85*, 573-597.

Bilanges, B., Posor, Y., and Vanhaesebroeck, B. (2019). PI3K isoforms in cell signalling and vesicle trafficking. Nat Rev Mol Cell Biol *20*, 515-534.

Braccini, L., Ciraolo, E., Campa, C.C., Perino, A., Longo, D.L., Tibolla, G., Pregnolato, M., Cao, Y., Tassone, B., Damilano, F.*, et al.* (2015). PI3K-C2gamma is a Rab5 effector selectively controlling endosomal Akt2 activation downstream of insulin signalling. Nat Commun *6*, 7400.

Burke, J.E., Triscott, J., Emerling, B.M., and Hammond, G.R.V. (2022). Beyond PI3Ks: targeting phosphoinositide kinases in disease. Nat Rev Drug Discov, 1-30.

Buwaneka, P., Ralko, A., Gorai, S., Pham, H., and Cho, W. (2021). Phosphoinositide-binding activity of Smad2 is essential for its function in TGF-beta signaling. J Biol Chem *297*, 101303.

Chen, M., Sun, T., Zhong, Y., Zhou, X., and Zhang, J. (2021). A Highly Sensitive Fluorescent Akt Biosensor Reveals Lysosome-Selective Regulation of Lipid Second Messengers and Kinase Activity. ACS Cent Sci *7*, 2009-2020.

Chen, Y., Sheng, R., Kallberg, M., Silkov, A., Tun, M.P., Bhardwaj, N., Kurilova, S., Hall, R.A., Honig, B., Lu, H.*, et al.* (2012). Genome-wide Functional Annotation of Dual-Specificity Protein- and Lipid-Binding Modules that Regulate Protein Interactions. Mol Cell *46*, 226-237.

Cho, W., and Stahelin, R.V. (2005). Membrane-protein interactions in cell signaling and membrane trafficking. Annu Rev Biophys Biomol Struct *34*, 119-151.

Di Paolo, G., and De Camilli, P. (2006). Phosphoinositides in cell regulation and membrane dynamics. Nature *443*, 651-657.

Dutta, D., Williamson, C.D., Cole, N.B., and Donaldson, J.G. (2012). Pitstop 2 is a potent inhibitor of clathrin-independent endocytosis. PLoS One *7*, e45799.

Falasca, M., Hughes, W.E., Dominguez, V., Sala, G., Fostira, F., Fang, M.Q., Cazzolli, R., Shepherd, P.R., James, D.E., and Maffucci, T. (2007). The role of phosphoinositide 3-kinase C2alpha in insulin signaling. J Biol Chem *282*, 28226-28236.

Fruman, D.A., Chiu, H., Hopkins, B.D., Bagrodia, S., Cantley, L.C., and Abraham, R.T. (2017). The PI3K Pathway in Human Disease. Cell *170*, 605-635.

Gillooly, D.J., Morrow, I.C., Lindsay, M., Gould, R., Bryant, N.J., Gaullier, J.M., Parton, R.G., and Stenmark, H. (2000). Localization of phosphatidylinositol 3-phosphate in yeast and mammalian cells. EMBO J *19*, 4577-4588.

Goulden, B.D., Pacheco, J., Dull, A., Zewe, J.P., Deiters, A., and Hammond, G.R.V. (2019). A high-avidity biosensor reveals plasma membrane PI(3,4)P2 is predominantly a class I PI3K signaling product. J Cell Biol *218*, 1066-1079.

Hammond, G.R., Fischer, M.J., Anderson, K.E., Holdich, J., Koteci, A., Balla, T., and Irvine, R.F. (2012). PI4P and PI(4,5)P2 are essential but independent lipid determinants of membrane identity. Science *337*, 727-730.

Hammond, G.R., Takasuga, S., Sasaki, T., and Balla, T. (2015). The ML1Nx2 Phosphatidylinositol 3,5-Bisphosphate Probe Shows Poor Selectivity in Cells. PLoS One *10*, e0139957.

Hasegawa, J., Strunk, B.S., and Weisman, L.S. (2017). PI5P and PI(3,5)P(2): Minor, but Essential Phosphoinositides. Cell Struct Funct *42*, 49-60.

Kim, E., Kim, D.H., Singaram, I., Jeong, H., Koh, A., Lee, J., Cho, W., and Ryu, S.H. (2018). Cellular phosphatase activity of C1-Ten/Tensin2 is controlled by Phosphatidylinositol-3,4,5-triphosphate binding through the C1-Ten/Tensin2 SH2 domain. Cell Signal *51*, 130-138.

Korolchuk, V.I., Saiki, S., Lichtenberg, M., Siddiqi, F.H., Roberts, E.A., Imarisio, S., Jahreiss, L., Sarkar, S., Futter, M., Menzies, F.M.*, et al.* (2011). Lysosomal positioning coordinates cellular nutrient responses. Nat Cell Biol *13*, 453-460.

Koseska, A., and Bastiaens, P.I.H. (2020). Processing Temporal Growth Factor Patterns by an Epidermal Growth Factor Receptor Network Dynamically Established in Space. Annu Rev Cell Dev Biol *36*, 359-383.

Koyama-Honda, I., Ritchie, K., Fujiwara, T., Iino, R., Murakoshi, H., Kasai, R.S., and Kusumi, A. (2005). Fluorescence imaging for monitoring the colocalization of two single molecules in living cells. Biophys J *88*, 2126-2136.

Li Chew, C., Lunardi, A., Gulluni, F., Ruan, D.T., Chen, M., Salmena, L., Nishino, M., Papa, A., Ng, C., Fung, J.*, et al.* (2015). In Vivo Role of INPP4B in Tumor and Metastasis Suppression through Regulation of PI3K-AKT Signaling at Endosomes. Cancer Discov *5*, 740-751.

Li, X., Wang, X., Zhang, X., Zhao, M., Tsang, W.L., Zhang, Y., Yau, R.G., Weisman, L.S., and Xu, H. (2013). Genetically encoded fluorescent probe to visualize intracellular phosphatidylinositol 3,5-bisphosphate localization and dynamics. Proc Natl Acad Sci U S A *110*, 21165-21170.

Lim, W.A., and Pawson, T. (2010). Phosphotyrosine signaling: evolving a new cellular communication system. Cell *142*, 661-667.

Liu, B.A., and Nash, P.D. (2012). Evolution of SH2 domains and phosphotyrosine signalling networks. Philos Trans R Soc Lond B Biol Sci *367*, 2556-2573.

Liu, S.L., Sheng, R., Jung, J.H., Wang, L., Stec, E., O'Connor, M.J., Song, S., Bikkavilli, R.K., Winn, R.A., Lee, D.*, et al.* (2017). Orthogonal lipid sensors identify transbilayer asymmetry of plasma membrane cholesterol. Nat Chem Biol *13*, 268-274.

Liu, S.L., Sheng, R., O'Connor, M.J., Cui, Y., Yoon, Y., Kurilova, S., Lee, D., and Cho, W. (2014). Simultaneous in situ quantification of two cellular lipid pools using orthogonal fluorescent sensors. Angew Chem Int Ed Engl *53*, 14387-14391.

Liu, S.L., Wang, Z.G., Hu, Y., Xin, Y., Singaram, I., Gorai, S., Zhou, X., Shim, Y., Min, J.H., Gong, L.W.*, et al.* (2018). Quantitative Lipid Imaging Reveals a New Signaling Function of Phosphatidylinositol-3,4-Bisphophate: Isoform- and Site-Specific Activation of Akt. Mol Cell *71*, 1092-1104 e1095.

Marat, A.L., and Haucke, V. (2016). Phosphatidylinositol 3-phosphates-at the interface between cell signalling and membrane traffic. EMBO J *35*, 561-579.

Marat, A.L., Wallroth, A., Lo, W.T., Muller, R., Norata, G.D., Falasca, M., Schultz, C., and Haucke, V. (2017). mTORC1 activity repression by late endosomal phosphatidylinositol 3,4-bisphosphate. Science *356*, 968-972.

Marshall, J.D.S., Whitecross, D.E., Mellor, P., and Anderson, D.H. (2019). Impact of p85alpha Alterations in Cancer. Biomolecules *9*.

Morris, G.M., Huey, R., Lindstrom, W., Sanner, M.F., Belew, R.K., Goodsell, D.S., and Olson, A.J. (2009). AutoDock4 and AutoDockTools4: Automated docking with selective receptor flexibility. J Comput Chem *30*, 2785-2791.

O'Boyle, N.M., Banck, M., James, C.A., Morley, C., Vandermeersch, T., and Hutchison, G.R. (2011). Open Babel: An open chemical toolbox. J Cheminform *3*, 33.

Park, M.J., Sheng, R., Silkov, A., Jung, D.J., Wang, Z.G., Xin, Y., Kim, H., Thiagarajan-Rosenkranz, P., Song, S., Yoon, Y.*, et al.* (2016). SH2 Domains Serve as Lipid-Binding Modules for pTyr-Signaling Proteins. Mol Cell *62*, 7-20.

Pawson, T. (2004). Specificity in signal transduction: from phosphotyrosine-SH2 domain interactions to complex cellular systems. Cell *116*, 191-203.

Posor, Y., Eichhorn-Gruenig, M., Puchkov, D., Schoneberg, J., Ullrich, A., Lampe, A., Muller, R., Zarbakhsh, S., Gulluni, F., Hirsch, E.*, et al.* (2013). Spatiotemporal control of endocytosis by phosphatidylinositol-3,4-bisphosphate. Nature *499*, 233-237.

Posor, Y., Jang, W., and Haucke, V. (2022). Phosphoinositides as membrane organizers. Nat Rev Mol Cell Biol *23*, 797-816.

Prinz, W.A., Toulmay, A., and Balla, T. (2020). The functional universe of membrane contact sites. Nat Rev Mol Cell Biol *21*, 7-24.

Riva, L., Yuan, S., Yin, X., Martin-Sancho, L., Matsunaga, N., Pache, L., Burgstaller-Muehlbacher, S., De Jesus, P.D., Teriete, P., Hull, M.V.*, et al.* (2020). Discovery of SARS-CoV-2 antiviral drugs through large-scale compound repurposing. Nature *586*, 113-119.

Rivero-Ríos, P., and Weisman, L.S. (2022). Roles of PIKfyve in multiple cellular pathways. Curr Opin Cell Biol *76*, 102086.

Schink, K.O., Raiborg, C., and Stenmark, H. (2013). Phosphatidylinositol 3-phosphate, a lipid that regulates membrane dynamics, protein sorting and cell signalling. Bioessays *35*, 900-912.

Schoenherr, C., Frame, M.C., and Byron, A. (2018). Trafficking of Adhesion and Growth Factor Receptors and Their Effector Kinases. Annu Rev Cell Dev Biol *34*, 29-58.

Sharma, A., Sun, J., Singaram, I., Ralko, A., Lee, D., and Cho, W. (2020). Photostable and Orthogonal Solvatochromic Fluorophores for Simultaneous In Situ Quantification of Multiple Cellular Signaling Molecules. ACS Chem Biol *15*, 1913-1920.

Sheng, R., Jung, D.J., Silkov, A., Kim, H., Singaram, I., Wang, Z.G., Xin, Y., Kim, E., Park, M.J., Thiagarajan-Rosenkranz, P.*, et al.* (2016). Lipids Regulate Lck Protein Activity through Their Interactions with the Lck Src Homology 2 Domain. J Biol Chem *291*, 17639-17650.

Singaram, I., Sharma, A., Pant, S., Lihan, M., Park, M.J., Pergande, M., Buwaneka, P., Hu, Y., Mahmud, N., Kim, Y.M.*, et al.* (2022). Targeting lipid-protein interaction to treat Syk-mediated acute myeloid leukemia. Nat Chem Biol.

Stahelin, R.V., Karathanassis, D., Bruzik, K.S., Waterfield, M.D., Bravo, J., Williams, R.L., and Cho, W. (2006). Structural and membrane binding analysis of the Phox homology domain of phosphoinositide 3-kinase-C2alpha. J Biol Chem *281*, 39396-39406.

Sun, J., Singaram, I., Soflaee, M.H., and Cho, W. (2020). A direct fluorometric activity assay for lipid kinases and phosphatases. J Lipid Res *61*, 945-952.

Tancini, B., Buratta, S., Delo, F., Sagini, K., Chiaradia, E., Pellegrino, R.M., Emiliani, C., and Urbanelli, L. (2020). Lysosomal Exocytosis: The Extracellular Role of an Intracellular Organelle. Membranes (Basel) *10*.

Thapa, N., Chen, M., Horn, H.T., Choi, S., Wen, T., and Anderson, R.A. (2020). Phosphatidylinositol-3-OH kinase signalling is spatially organized at endosomal compartments by microtubule-associated protein 4. Nat Cell Biol *22*, 1357-1370.

Tillberg, P.W., Chen, F., Piatkevich, K.D., Zhao, Y., Yu, C.C., English, B.P., Gao, L., Martorell, A., Suk, H.J., Yoshida, F.*, et al.* (2016). Protein-retention expansion microscopy of cells and tissues labeled using standard fluorescent proteins and antibodies. Nat Biotechnol *34*, 987-992.

Vines, J.H., Buckley, C.M., Maib, H., Gueho, A., Soldati, T., Murray, D., and King, J.S. (2022). A PI(3,5)P2 probe reveals PIKfyve is required for Rab7 acquisition and the delivery and fusion of early macropinosomes to phagosomes. bioRxiv, 2022.2009.2019.508510.

von Kleist, L., Stahlschmidt, W., Bulut, H., Gromova, K., Puchkov, D., Robertson, M.J., MacGregor, K.A., Tomilin, N., Pechstein, A., Chau, N.*, et al.* (2011). Role of the clathrin terminal domain in regulating coated pit dynamics revealed by small molecule inhibition. Cell *146*, 471-484.

Wang, S., Jia, L., Zhou, H., Shi, W., and Zhang, J. (2009). Knockdown of caveolin-1 by siRNA inhibits the transformation of mouse hepatoma H22 cells in vitro and in vivo. Oligonucleotides *19*, 81-88.

Wheeler, M., and Domin, J. (2001). Recruitment of the class II phosphoinositide 3-kinase C2beta to the epidermal growth factor receptor: role of Grb2. Mol Cell Biol *21*, 6660-6667.

Willox, A.K., Sahraoui, Y.M., and Royle, S.J. (2014). Non-specificity of Pitstop 2 in clathrin-mediated endocytosis. Biol Open *3*, 326-331.

Yoon, Y., Lee, P.J., Kurilova, S., and Cho, W. (2011). In situ quantitative imaging of cellular lipids using molecular sensors. Nat Chem *3*, 868-874.

Zhang, M., Jang, H., and Nussinov, R. (2021). PI3K Driver Mutations: A Biophysical Membrane-Centric Perspective. Cancer Res *81*, 237-247.

Zhang, X., Vadas, O., Perisic, O., Anderson, K.E., Clark, J., Hawkins, P.T., Stephens, L.R., and Williams, R.L. (2011). Structure of lipid kinase p110beta/p85beta elucidates an unusual SH2-domain-mediated inhibitory mechanism. Mol Cell *41*, 567-578.

FIGURE LEGENDS

Fig. 1. Membrane binding properties of the p85α-cSH2 domain and p85α-cSH2-derived PI(3,5)P_2 sensor.

A. PtdInsP selectivity of p85α-cSH2 determined by SPR analysis. POPC/POPS/PtdInsP (77:20:3 in mole ratio) LUVs were coated on the L1 sensor chip and 200 nM p85α-cSH2 was injected into the flow cell for binding measurements. PI(3)P and PI(4)P yielded essentially the same responses.

B. The structure of p85α-cSH2 (protein data bank ID = 1H9O) shown in a surface diagram with a docked PI(3,5)P_2 molecule (stick representation). Mutated residues in this study are shown in space-filling representation (carbon in green, oxygen in red, nitrogen in blue and sulfur in orange) and labeled. The molecule is oriented with its potential membrane binding surface facing upward. The dotted cyan line indicates a putative location of the membrane surface. A putative PI(3,5)P_2 binding site and the reported pY binding pocket are indicated by red and green arrows, respectively.

C. A basic principle of ratiometric PI(3,5)P_2 imaging. The ratiometric PI(3,5)P_2 sensor, WCB-*e*p85α-cSH2, contains a bright and photostable solvatochromic fluorophore WCB ((*E*)-3-((((7-(diethylamino)-9,9-dimethyl-9*H*-fluoren-2-yl)methylene)amino)oxy)-2-hydroxypropyl acrylate) that undergoes a hypsochromic shift (or blue shift) in fluorescence emission upon binding to membranes (see **Fig. 1E**).

D. Steps of a ratiometric PI(3,5)P_2 sensor development and cellular ratiometric imaging. See **Fig. S2A** for detailed procedure for sensor development and characterization.

E. PtdInsP selectivity of WCB-*e*p85α-cSH2. Fluorescence emission spectra of WCB-*e*p85α-cSH2 (500 nM) in response to binding to 50 μM POPC/POPS (80:20) (labeled PS in black) and POPC/POPS/PtdInsP (77:20:3) (each PtdInsP separately labeled and colored) LUVs were obtained spectrofluorometrically with the excitation wavelength set at 380 nm. The spectrum of sensor without lipid is shown in orange at the bottom.

F. Fluorescence emission spectra of WCB-*e*p85α-cSH2 in response to binding to POPC/POPS/PI(3,5)P_2 (80–*x*/20/*x*: x = 0–2 mol%) LUVs. The spectra were obtained spectrofluorometrically with the excitation wavelength set at 380 nm. The intensity values were normalized using the maximal intensity of the free sensor as the reference. The emission spectrum of the sensor (orange) was blue-shifted upon vesicle binding and its maximal emission intensity at 440 nm was increased as the PI(3,5)P_2 concentration varied from 0, 0.5, 1, 1.5, and 2 mol% from bottom to top.

G. The giant unilamellar vesicle (GUV) binding curve of WCB-*e*p85α-cSH2 determined by fluorescence microscopy. Lipid compositions of GUVs were POPC/POPS/PI(3,5)P_2 (80-x/20/x: x = 0-2 mol%). The binding isotherm was analyzed by non-linear least squares analysis using a modified Langmuir equation: $y = y_{min} + (y_{max} - y_{min})/(1 + K_d / [PI(3,5)P_2])$ where K_d, y_{max} and y_{min} are PI(3,5)P_2 concentrations ([PI(3,5)P_2]) yielding half maximal binding, the maximal and minimal y values. Half maximal vesicle binding was achieved with [PI(3,5)P_2] = 0.27 ± 0.02 mol%. This plot was used as a ratiometric calibration curve for converting experimentally observed F_B/F_G values to cellular [PI(3,5)P_2].

Fig. 2. Quantitative cellular imaging of PI(3)P and PI(3,5)P_2.

A. Subcellular distribution of microinjected WCB-*e*p85α-cSH2 in HeLa cells. The blue channel image shows intracellular punctate distribution of the sensor. The scale bar and dotted lines show 10 μm and cell outlines, respectively. The same pattern was observed in HEK293 cells. **B.** A spatially resolved PI(3,5)P_2 profile calculated from the two-channel cross-sectional ratiometric image of a representative HeLa cell (n >30) at steady-state. The z-axis scale indicates the PI(3,5)P_2 concentration ([PI(3,5)P_2]) (mol%). A pseudo-coloring scheme with red and blue representing the highest (0.2 mol%) and the lowest (0 mol%) concentration, respectively, is used to illustrate the spatial PI(3,5)P_2 heterogeneity. Scale bars in **A** and **B** indicate 10 μm. Essentially the same results were obtained in HEK293 cells. **C.** Cellular metabolism of PI(3,5)P_2. All lipid kinases and phosphatase involved in the metabolism are shown in green and red, respectively. Available small-molecule inhibitors are indicated in blue. **D.** The effects of inhibiting lipid kinases and phosphatases on spatially averaged [PI(3,5)P_2] in HEK293 cells before PDGF stimulation. Cells were pretreated with a PIKFyve inhibitor, apilimod (1 μM, 24 h) or YM201636 (0.8 μM, 24 h), siRNAs (KD) for PIKFyve, a Vps34 inhibitor SAR405 (10 μM, 24 h), and siRNAs for Vps34, PI3KC2α, PI3KC2β, and INPP4B, respectively. Apilimod and YM201636 yielded the same results. All siRNA treatments were for 48 h. $p < 0.0001$ for all data set (e.g., untreated versus SAR405). **E.** An increase in spatially averaged [PI(3,5)P_2] in HEK293 cells at 12 min post PDGF stimulation (50 ng/ml). Averages and S.D.'s are shown. $p < 0.0001$. **F.** The effects of inhibiting lipid kinases and phosphatases on spatially averaged [PI(3,5)P_2] in HEK293 cells 12 min after PDGF stimulation (50 ng/ml). See **Fig. 2D** for conditions. Apilimod and YM201636 yielded the same results. $p < 0.0001$ for all data set (e.g., untreated versus SAR405). For **Fig. 2D** and **2F**, [PI(3,5)P_2]

values represent averages ± S.D.'s from four independent determinations (n = 30-35). **G.** Time-dependent changes of the spatially averaged [PI(3,5)P_2] in HEK293 (blue) and PI3KC2β-null HEK293 (KO) (red), and PI3KC2β-null HEK293 cells after reintroduction of PI3KC2β WT (KO + WT-KI) (orange) after PDGF stimulation (50 ng/ml). [PI(3,5)P_2] values (averages ± S.D.'s from three independent determinations; n = 30-35) were determined at different time intervals. **H.** Time-dependent changes of the spatially averaged PI(3)P concentration ([PI(3)P]) (n = 30-35) in HEK293 cells after PDGF stimulation (50 ng/ml). 10 μM SAR405 (24 h) was used for Vps34 inhibition.

Fig. 3. Time courses of PIP_3 formation and disappearance at the plasma membrane

A. PDGF (50 ng/ml)-stimulated changes in the spatially averaged PIP_3 concentration ([PIP_3]) at the PM of HEK293 cells. HEK293 cells were either untreated (blue) or pre-treated with 0.8 μM (24 h) YM201636 (cyan), PIKfyve siRNA (KD) and PI3KC2β siRNA (red), respectively. **B.** PDGF-stimulated changes in [PIP_3] at the PM of HEK293 cells (blue) and PI3KC2β-null (KO) HEK293 cells before (red) and after adding back (KI) PI3KC2β WT (orange). **C**. The time course of PDGF-stimulated phosphorylation of S473 of endogenous Akt1 in HEK293 cells before (left) and after (middle) YM201636 treatment and in PI3KC2β-null HEK293 cells (right). Representative western blots (n = 3) show pS473-Akt1and total Akt1 detected by immunoblot (IB) with the pS473-Akt1-specific and Akt1-specific antibodies, respectively. Glyceraldehyde 3-phosphate dehydrogenase (GAPDH) was used as a loading control. **D.** Quantification of **Fig. 3C**. The ratio of the gel density of the pS473-Akt1 band to that of the total Akt band is plotted as a function of time. All siRNA treatments were for 48 h. Data represent averages ± S.D.'s from three independent determinations

Fig. 4. Inhibition of the enzyme activity and plasma membrane binding of PI3Kα by PI(3,5)P_2.

A. *cis*- versus *trans*-vesicular inhibition of Class I PI3K by PI(3,5)P_2**.** For *cis*-vesicular inhibition, PI(3,5)P_2 is added to the same vesicles where PI(4,5)P_2 is present whereas for *trans*-vesicular inhibition, PI(3,5)P_2-containing vesicles were mixed with PI(4,5)P_2-containing vesicles. *Cis* inhibition would indicate that PI(3,5)P either competes with PI(4,5)P_2 for the catalytic sites of PI3K or causes allosteric inhibition. Conversely, *trans* inhibition would support the PI3K-displacement model. **B.** The kinetics of PI3Kα-catalyzed phosphorylation of PI(4,5)P_2 in

POPC/POPS/PI(4,5)P_2 (77:20:3) LUVs in the presence of POPC/POPS/PI(3,5)P_2 (80-*x*/20/*x*; *x* = 0, 0.5, 1, 1.5, 2, 2.5 and 3 mol%) LUVs. DAN-*e*ENTH (500 nM) was incubated with 50 μM each of the two LUVs for 1 min, and then 50 nM PI3Kα (p110α-p85α-WT), 10 μM pY2 peptide, and 100 μM ATP were added to initiate the reaction. **C.** The same measurement was performed with the p110α-p85α-K653A mutant. **D.** Concentration-dependent *trans*-vesicular inhibition of PI3Kα WT and mutants by PI(3,5)P_2. Relative enzyme activity was determined by calculating initial rates of PI(4,5)P_2 phosphorylation by PI3Kα WT (blue), K653A (red), G376R (green), K379E (cyan), and R642L (orange) from **Fig. 4B-C**, and **Fig S10A-C** and normalized them against that of PI3Kα WT in the absence of PI(3,5)P_2 (= 0.75 μM/s). Each data point represents average ± S.D. from three independent measurements. **E.** Direct visualization of *trans*-vesicular movement of activated EGFP-PI3Kα (green) from POPC/POPS/PI(4,5)P_2/1,2-dioleoyl-sn-glycero-3-phosphoethanolamine-N-(lissamine rhodamine B sulfonyl) (Rh-PE) (67:20:3:10) GUVs (red) to POPC/POPS/PI(3,5)P_2 (80- *x*:20*x*, *x* = 0-3) GUVs (no color) by fluorescence microscopic imaging. The orange color in merged images indicates colocalization of EGFP-PI3Kα and PI(4,5)P_2 GUVs. Differential interference contrast (DIC) images of GUVs are shown in the bottom row to better illustrate relative locations of GUVs and EGFP-PI3Kα. These images are representative of similar images collected in three independent measurements (*n* >100). Scale bars indicate 10 μm. **F.** Quantification of **Fig. 4E**. Relative EGFP intensity on PI(4,5)P_2 (or PI(3,5)P_2) GUVs was calculated by normalizing the total EGFP fluorescence intensity on these GUVs in the presence of GUVs with varying PI(3,5)P_2 contents against that in the absence of PI(3,5)P_2 GUVs. EGFP fluorescence intensity on GUVs were background corrected against the signal in the absences of EGFP-PI3Kα.

Fig. 5. Subcellular localization of PI3Kα in response to PDGF stimulation. A. Kinetics of PDGF-stimulated (50 ng/ml) PM localization of PI3Kα WT (blue) and K653A (red) in p110α-null MEF cells. The endogenous p85α and p85β of MEF cells were suppressed by siRNAs and human EGFP-tagged PI3Kα WT (p110α-p85α-WT) (blue) and PI3Kα-K653A (p110α-p85α-K653A) (red) were exogenously expressed. PI3Kα WT was also inhibited by 0.8 μM YM201636 (24 h) (cyan). PM dwell time was calculated as $ln2/k$ where k is the dissociation rate constant from PM. Data points indicate averages ± S.D.'s from five independent measurements (*n*>250 cells). **B.** Degree of PM localization of endogenous PI3Kα before (blue) and after siRNA-mediated PIKfyve

knockdown (KD) (cyan) and inhibition by 30 μM Pitstop2 for 15 min (red). Relative population of PI3Kα on PM was calculated as $I_{PM}/(I_{PM} + I_{cytosol})$ where indicated the fluorescence intensity at the PM and cytosol, respectively. Endogenous PI3Kα was stained with p110α-specific antibody. Data points indicate averages ± S.D.'s from three independent determinations (*n* >30 cells). **C.** Time-dependent lysosome localization of endogenous PI3K with and without PIKFyve knockdown (KD) or Pitstop2 treatment was determined by monitoring the Pearson's correlation coefficient between p85 and LAMP1 at different times. For HEK293 cells, $p = 0.904$ (5 min), <0.0001 (10 min), 0.00029 (20 min); For HEK293 + PIKFyve KD, $p = 0.562$ (5 min), 0.249 (10 min), 0.150 (20 min); For HEK293 + Pitstop2, $p = 0.114$ (5 min), <0.0001 (10 min), 0.00021 (20 min). **D.** The same as **Fig. 4C** except that expansion microscopy data (see **Fig. S9D**) were analyzed. For HEK293 cells, $p = 0.148$ (5 min), <0.0001 (10 min), <0.0001 (20 min); For HEK293 + YM201636, $p = 0.053$ (5 min), 0.05 (10 min), 0.138 (20 min). **E.** Time-dependent early endosome localization of endogenous PI3K (no treatment, with 30 μM Pitstop2, and with PIKFyve KD) was determined by monitoring the Pearson's correlation coefficient between p85 and EEA1 at different times. For HEK293 cells, $p = 0.255$ (5 min), 0.397 (10 min), 0.743 (20 min); For HEK293 + PIKFyve KD, $p = 0.368$ (5 min), 0.746 (10 min), 0.758 (20 min); For HEK293 + Pitstop2, $p = 0.957$ (5 min), 0.965 (10 min), 0.716 (20 min). Endogenous PI3K was stained with p85 antibody. Data points indicate averages ± S.D.'s from three independent determinations (n >20 cells).

Fig. 6. Effects of p85α mutations on kinetics of PIP_3 formation at the plasma membrane. A. PDGF-stimulated changes in [PIP_3] at the PM of HEK293 cells (blue) and p85α/β-double knockdown HEK293 cells before (red) and after reintroducing (KI) mouse p85α WT (orange) or p85α-K653A (green). **B.** PDGF-stimulated changes in [PIP_3] at the PM of p85α/β-double knockdown HEK293 cells expressing a mouse p85α mutant: K379E (green), R642L (orange), N564D (blue), G376R (red), or R461A (pink). [PIP_3] values at different time points represent averages ± S.D.'s from four independent determinations (*n* >20 cells). **C.** A hypothetical model of $PI35P_2$-mediated feedback inhibition of Class I PI3K signaling. In response to growth factor stimulation (e.g., PDGF), Class I PI3K is recruited to the activated growth factor receptor and activated. The activated PI3K phosphorylates $PI(4,5)P_2$ to PIP_3 in the plasma membrane (PM), which is then dephosphorylated by SHIP2 to $PI(3,4)P_2$. Growth factor stimulation also activates Class II PI3KC2β in the PM by an unknown mechanism. The activated PI3KC2β phosphorylates

PI to PI(3)P primarily in early endosomes (EE). Constitutively active PIKfyve converts PI3KC2β-produced PI(3)P to PI(3,5)P_2 mainly in late endosomes (LE) and lysosomes (Lyso), which inhibits Class I PI3K by specifically binding to p85 SH2 domains and thereby displacing the PI3K molecules from the PM. This feedback inhibition by PI(3,5)P_2 terminates growth factor-induced PI3K activation.

STAR*METHODS

CONTACT FOR REAGENT AND RESOURCE SHARING

Further information and requests for resources, materials and reagents should be directed to and will be fulfilled by the Lead Contact Wonhwa Cho (University of Illinois Chicago, Email: wcho@uic.du).

EXPERIMENTAL MODEL AND SUBJECT DETAILS

Cell lines

HEK293, NIH 3T3, MEF, and HeLa cells were purchased from ATCC and cultured in DMEM containing 4.5 g/l D-glucose, L-glutamine, 110 mg/l sodium pyruvate, 10% heat-inactivated FBS, 100 U/ml penicillin, and 100 μg/ml streptomycin (Gibco). Cells were routinely tested for mycoplasma contamination.

METHOD DETAILS

Materials

See Key Resources Table.

REAGENT OR RESOURCE	SOURCE	IDENTIFIER
Antibodies		
pS473-Akt	Cell Signaling Technologies	Catalog No.: 4060
Akt1	Cell Signaling Technologies	Catalog No.: 2938
glyceraldehyde 3-phosphate dehydrogenase (GAPDH)	Cell Signaling Technologies	Catalog No.: 5174
PI3 Kinase p85 Antibody	Cell Signaling Technologies	Catalog No.: 4292
PI3 Kinase Class II α (D3Q5B) Rabbit mAb	Cell Signaling Technologies	Catalog No.:12402
Anti-PIK3C2B	abcam,	Catalog No.: ab231122
INPP4b (D19B9) Rabbit mAb	Cell Signaling Technologies	Catalog No.:8450
Lamp1	Cell Signaling Technologies	Catalog No.: 15665
EEA1	Cell Signaling Technologies	Catalog No.: 48453

PIKfyve (mouse)	SCBT	Cat# sc-100408
PI3 Kinase Class III (D4E2) Rabbit mAb	Cell Signaling Technologies	Catalog No.:3358
PI3 Kinase p110α (C73F8) Rabbit mAb	Cell Signaling Technologies	Catalog No.:4249
Goat anti-Mouse IgG (H+L) Highly Cross-Adsorbed Secondary Antibody, Alexa Fluor™ 488	Thermo Fisher Scientific	Catalog # A-11029
Goat anti-Rabbit IgG (H+L) Cross-Adsorbed Secondary Antibody, Alexa Fluor™ 568	Thermo Fisher Scientific	Catalog # A-11011
Bacterial and virus strains		
PIK3CA-WT (pFastBac)	Addgene	Plasmid #16644
pFastBac1 PIK3R1	Addgene	Plasmid #17743
Chemicals, Peptides, Recombinant Proteins, and other supplies		
YM201636	AdooQ BioSciences	Catalog No.: A11064
Apilimod	MedKoo Biosciences	Catalog No.: 407105
SAR405	Cayman Chemical	Catalog No.: 16979
AS1938909	Echelon Biosciences	Catalog No.: B-0343
PITSTOP2	MedChemExpress	Catalog No.: HY-115604
Human platelet-derived growth factor (PDGF)-BB	PEPROTECH	Catalog No.: 100-14B
Human epidermal growth factor (EGF)	Sigma-Aldrich	Catalog No.: E9644
pY2 peptide (ESDGGpYMDMSKDESIDpYVPMLDMKGDIKYA)	Cho lab	N/A
pY peptide (F-Ahx-ADNDpYIIPLPD)	AlanScientific	custom-purchased
Acrylodan	Cho lab	N/A
WCB	Cho lab	N/A
Ni-NTA resin	Marvelgent Biosciences Inc	Catalog No.: 11-0224-100
Glutathione resin	Genscript	Catalog No.: L00206
IGF1	PEPROTECH	Catalog No.: 100-11
Pierce™ ECL Western Blotting Substrate	Thermo Scientific	Catalog No.: 32109

Acryloyl-X SE	Thermo Fisher	Catalog No.: A20770
sodium acrylate	Pfaltz&Bauer	Catalog No.: S03880
acrylamide	Millipore Sigma	Catalog No.: A9099
N,N'-Methylenebisacrylamide	Millipore Sigma	Catalog No.: 146072
ammonium persulfate (APS)	Millipore Sigma	Catalog No.: A3678
tetramethylethylenediamine (TEMED)	Millipore Sigma	Catalog No.: T7024
4-hydroxy-2,2,6,6-tetramethylpiperidin-1-oxyl (4HT)	Millipore Sigma	Catalog No.: 00375
Proteinase K	New England Biolabs	Catalog No.: P8107S
Normal Goat Serum	jacksonimmuno	Catalog No.: 005-000-121
DAPI	Millipore Sigma	Catalog No.: D9542
poly-L-lysine	Sigma	Catalog No.:A-005-C
Corning® cover glasses	Sigma	Catalog No.: 2850-22
24 well coverslips	Neuvitro Corporation	Catalog No.: CG-12
L1 sensor chip	GE healthcare	Catalog No.: 29-1049-93
Nuclepore Track-Etch membrane (0.1μm)	Cytiva (Whatman)	Catalog No.: 7514682
jetPRIME® DNA and/or siRNA transfection reagent	Genesee Scientific Corporation	Catalog No.: 55-131
Experimental Models: Cell Lines		
HEK 293	ATCC	CRL-1573
HeLa	ATCC	CCL-2
NIH 3T3	ATCC	CRL-1658
HEK 293-PI3KC2β -null HEK 293	Volker Haucke lab	N/A
PTEN-null MEF	Nissim Hay lab	N/A
p110α-null MEF	Jean Zhao lab	N/A
Spodoptera frugiperda (Sf9)	ATCC	CRL-1711
BTI-Tn-5B1-4 (High Five)	Cho lab	N/A
Oligonucleotides		
mm.Ri.Pik3c2a.13.1	IDT	REF #: 274361311
hs.Ri.PIK3C2A.13.2	IDT	REF #: 410454389
mm.Ri.Pik3c2b.13.1	IDT	REF #: 274361314
hs.Ri.PIK3C2B.13.2	IDT	REF #: 410454392

hs.Ri.PIK3C3.13.1	IDT	REF #: 410454398
hs.Ri.PIK3C3.13.2	IDT	REF #: 410454395
hs.Ri.PIKFYVE.13.1	IDT	REF #: 410454401
mm.Ri.Pik3r2.13.2	IDT	REF #: 410454404
mm.Ri.Pik3r2.13.3	IDT	REF #: 410454407
hs.Ri.INPP4B.13.1	IDT	REF #: 410454410
hs.Ri.PIKFYVE.13.2	IDT	REF #: 410454413
inpp4b siRNA	IDT	REF #: 219906787
mm.Ri.Pik3r1.13	IDT	REF #: 298332166
mm.Ri.Pik3r2.13.1	IDT	REF #: 298332163
Lipids		
1-Palmitoyl-2-oleoyl-sn-glycero-3-phosphocholine-d82 (POPC) (	Avanti Polar Lipids.	Catalog No.: 860360
1-palmitoyl-2-oleoyl-sn-glycero-3-phosphoethanolamine (POPE)	Avanti Polar Lipids.	Catalog No.: 850757
1-palmitoyl-2-oleoyl-sn-glycero-3-phospho-L-serine (sodium salt) (POPS)	Avanti Polar Lipids.	Catalog No.: 840034
liver phosphatidylinositol (PI)	Avanti Polar Lipids.	Catalog No.: 840042
cholesterol	Avanti Polar Lipids.	Catalog No.: 700100
Rd-PE	Cho lab	
PtdIns-(3)-P_1 (1,2-dipalmitoyl) (ammonium salt)	Cayman Chemical Co.	Catalog No.: 64921
PtdIns-(4)-P_1 (1,2-dipalmitoyl) (ammonium salt)	Cayman Chemical Co.	Catalog No.: 64923
PtdIns-(5)-P_1 (1,2-dipalmitoyl) (ammonium salt)	Cayman Chemical Co.	Catalog No.: 64925
PtdIns-(4,5)-P2 (1,2-dipalmitoyl) (sodium salt)	Cayman Chemical Co.	Catalog No.: 10008115
PtdIns-(3,4)-P2 (1,2-dipalmitoyl) (sodium salt)	Cayman Chemical Co.	Catalog No.: 64922
PtdIns-(3,5)-P2 (1,2-dipalmitoyl) (sodium salt)	Cayman Chemical Co.	Catalog No.: 10008398
PtdIns-(3,4,5)-P3 (1,2-dipalmitoyl) (sodium salt)	Cayman Chemical Co.	Catalog No.: 64920
Recombinant DNA		
Lamp1-mCherry	Cho lab	N/A
Rab5-iRFP	Cho lab	N/A
Rab7-iRFP	Cho lab	N/A
EEA1-eGFP	Cho lab	N/A

p85α-cSH2-eGFP	Cho lab	N/A
p85-cSH2	Cho lab	N/A
EEA1-FYVE-V21C	Cho lab	N/A
*e*ENTH	Cho lab	N/A
MyoX-tPH	Cho lab	N/A
EGFP-tagged-p110α	Cho lab	N/A
p85α	Cho lab	N/A
Software and Algorithms		
ImageJ (1.53t)	Open Source Software	https://imagej.nih.gov/ij/
ImageJ Plugin coloc2 (3.0.5)	Open Source Software	https://imagej.nih.gov/ij/
ImageJ Plugin dotted line	Open Source Software	https://imagej.nih.gov/ij/
MATLAB (2021b)	UIC	https://webstore.illinois.edu/shop/product.aspx?zpid=4402
PyMOL	Schrödinger, LLC	https://pymol.org/2/
Image-Pro Plus7 (v6.0)	Mediacybernetics	https://www.mediacy.com/
Synergy Kaleidagraph (v.5.0)	Synergy Software	https://www.synergy.com/

Class I PI3K expression and purification

p85α-cSH2 was subcloned into the pESETB-eGFP vector for bacterial expression as an EGFP-tagged protein for SPR studies. Two subunits of PI3Kα, p110α and p85α, were co-expressed in insect cells as described previously for PI3Kβ (Sun et al., 2020). Recombinant baculoviruses for p110α and p85α were amplified in *Spodoptera frugiperda* (Sf9) cells. BTI-Tn-5B1-4 (High Five) suspension insect cells (2 x 10^6 cells/ml) were then co-infected with p110α and p85α baculoviruses (MOI ratio = 1:3) for protein expression. Cells were harvested 72 h after infection. Cell pellets were suspended in a buffer containing 50 mM Tris, 300 mM NaCl, 10 mM imidazole, 1 mM tris(2-carboxyethyl) phosphine (TCEP), 1 mM phenylmethylsulphonyl fluoride (PMSF) (PH 7.9) and lysed using a hand-held homogenizer (Tissue Grinder Size C; Thomas Scientific). After centrifugation of the homogenate, the supernatant was incubated with the Ni-NTA resin for 2 h. The resin was then poured into a small column and washed with Buffer A (20 mM Tris-HCl, 300 mM NaCl, 10 mM imidazole (pH 7.9)) and then Buffer B (20 mM Tris-HCl, 300 mM NaCl, 40 mM imidazole (pH 7.9)). The protein was eluted with the elution buffer (20 mM Tris-HCl, 160

mM NaCl, 300 mM imidazole, 1 mM PMSF, 0.5 mM TCEP, 50 mM arginine, 50 mM glutamic acid (pH 7.9)).

Preparation of the PI(3,5)P_2 sensor

For sensor preparation, p85α-cSH2 was subcloned into the pET-30a(+) vector and sequentially mutated. The engineered PI(3,5)P_2 sensor (WCB-*e*p85α-cSH2) was expressed as a His_6-tagged proteins in *E. coli* BL21 RIL codon plus cells. Protein expression was induced at 19°C with 0.5 mM (final concentration) isopropyl β-d-1-thiogalactopyranoside when the optical density of the media reached 0.6-0.8. Cells were harvested and cell pellets were suspended in lysis buffer containing 50 mM Tris, 300 mM NaCl, 10 mM imidazole, TCEP, 1 mM PMSF (PH 7.9) and lysed by sonication. The supernatant was incubated with the Ni-NTA resin after centrifugation of the homogenate. The resin mixture was then poured into a small column and washed Buffer A (20 mM Tris-HCl, 300 mM NaCl, 10 mM imidazole (pH 7.9)). After the resin became clear, the buffer solution was replaced by 5 ml of labeling buffer (50 mM Tris-HCl, 300 mM NaCl, 1 mM TCEP, 50 mM arginine, 50 mM glutamic acid (pH 8.0)). After adding 100 µl of WCB (10 mg/ml in dimethylsulfoxide (DMSO)), the mixture was gently shaken at room temperature for 2 h. The resin was first washed with Buffer A with 5% DMSO until the free dye was completely removed and then Buffer B (20 mM Tris-HCl, 300 mM NaCl, 40 mM imidazole (pH 7.9)). The sensor was eluted with the elution buffer (20 mM Tris-HCl, 160 mM NaCl, 300 mM imidazole, 0.5 mM TCEP, 50 mM arginine, 50 mM glutamic acid (pH 7.9)). The purity of the sensor was confirmed by the sodium dodecylsulfate polyacrylamide gel electrophoresis and the protein concentration was determined by the Bradford assay. The activity of the purified sensor was routinely checked by a quick three-point fluorometric measurement at 470 nm (F_{470}) and at 530 nm (F_{530}) using e.g., 10, 50, and 100 µM of POPC/POPS/PI(3,5)P_2 (77:20:3) vesicles. The ratio (F_{470}/F_{530}) values from these measurements should lie within the 10% range of the standard calibration curves.

Preparation of the PI(3)P and PI(4,5)P_2 sensors

EEA1-FYVE-V21C was subcloned into the pGEX4T-1 vector and expressed as a GST-tagged protein in BL21 (DE3) pLysS cells. The expressed protein was extracted from the cells as described above. The cell supernatant was mixed with the glutathione resin and incubated with 100 µl of acrylodan solution (1 mg/ml in DMSO) in 5 ml of 20 mM Tris buffer, pH 7.4, containing

160 mM NaCl and 0.5 mM TCEP for 2h at room temperature with gentle mixing. Resins were washed with 100 ml of 20 mM Tris buffer with 160 mM NaCl at pH 7.4 with 5% DMSO. After washing, DAN-*e*EEA1 was incubated with 1 µl of thrombin (Invitrogen) in 1 ml of thrombin cleavage buffer (20 mM Tris, 160 mM NaCl, 25 mM $CaCl_2$, 1 mM dithiothreitol at pH 8) overnight at 4°C. The eluted protein was used immediately used for imaging. The PI(4,5)P_2 sensor, DAN-*e*ENTH, and the PIP_3 sensor, DAN-eMyoX-tPH, were prepared as described previously (Sun et al., 2020; Yoon et al., 2011).

Surface plasmon resonance (SPR) analysis

All SPR measurements were performed at 23°C in 20 mM Tris, pH 7.4, containing 0.16 M NaCl using a lipid-coated L1 chip in the BIACORE X100 system (Cytiva) as described previously (Buwaneka et al., 2021; Park et al., 2016). LUVs of POPC/POPS/PI(3,5)P_2 (77:20:3) and POPC/POPS (80:20) were used as the active surface and the control surface, respectively. Equilibrium SPR measurements were carried out at a flow rate of 5 µl/min to allow sufficient time for the R values of the association phase to reach near-equilibrium values (R_{eq}). Sensorgrams were analyzed assuming a Langmuir-type binding between the protein (P) and protein binding sites (M) on vesicles (that is, P + M↔PM). The R_{eq} values were plotted against the protein concentrations (P_o), and the K_d was determined by nonlinear least squares analysis of the binding isotherm using the equation, $R_{eq} = R_{max}/(1 + K_d/P_o)$. For kinetic SPR measurements, the flow rate was maintained at 30 µl/min for both association and dissociation phases.

Molecular docking analysis

The binding modes of the PI(3,5)P_2 and p85-cSH2 were calculated using Autodock4 software (The Scripps Research Institute, La Jolla, USA) (Morris et al., 2009). 1,2-dioleoyl derivative of PI(3,5)P_2 was drawn and energy-minimized with Chem Draw ultra and Chem 3D ultra, respectively. The structure was saved as sdf file and protein data bank (PDB) file was generated using OpenBabel2.3.1 software (O'Boyle et al., 2011). The crystal structure of p85-cSH2 (PDB ID: IH9O) was used for docking analysis. The macromolecule was then prepared by removing the water molecules and adding hydrogens and Kollman charges and saved in PDBQT format for the Autodock4 program. A cube shape grid coordinates (dimension: x = 70, y = 70, z = 70 and center x = -0.861, y = 12.582, z = 5.833) were set to cover the binding site of p85-cSH2. To run the

docking, the parameters were kept as default. Finally, the generated dlg file was analyzed and the lowest energy binding conformation was considered as the best docking pose. The docking pose was exported and illustrated using PyMOL (The PyMOL Molecular Graphics System, Version 2.0 Schrödinger, LLC).

In vitro PI3K activity assay

All cuvette-based continuous PI3K activity assays were performed with the FluoroLog3 spectrofluorometer at 37ºC in a 1 ml quartz cuvette (Hellma Analytics) as described previously (Sun et al., 2020). For the PI3K activity assay, 874 µl of 20 mM Tris buffer, pH 7.4, containing 0.16 M NaCl was mixed with 100 µl of POPC/POPS/PI(4,5)P_2 (77:20:3 in mole%; 400 µg/ml) LUVs at the indicated concentration, 5 µl of 50 µM DAN-eENTH (Yoon et al., 2011) (final concentration: 500 nM), 10 µl of 0.1 mM pY2 peptide (final concentration: 500 nM), and 10 µl of 0.1 M ATP (final concentration: 0.1 mM). The reaction was initiated by adding 10 nM of enzyme solution to the mixture continuously monitored by measuring the blue-shifted emission of the sensor at 470 nm with the excitation wavelength set at 380 nm.

Cell culture and stimulation

HEK293 (or other) cells were seeded into 50 mm round glass–bottom plates and grown at 37ºC in a humidified atmosphere of 95% air and 5% CO_2 in Dulbecco's modified Eagle's medium (DMEM) with 4.5 g/l D-glucose , L-glutamine, 110 mg/l sodium pyruvate containing 10% heat-inactivated FBS, 100 U/ml penicillin, and 100 µg/ml streptomycin (Gibco) and cultured in the Corning cover glasses for 24 h before lipid quantification. All cell lines were cultured bi-weekly and stocks of cell lines were passaged no more than ten times for use in experiments. Growth factor stimulation was performed as described (Liu et al., 2018). Briefly, HEK293 (or other cells) were stimulated with 50 ng/ml PDGF-BB, EGF or IGF. Serum starvation was not employed because some inhibitors, such as YM201636, caused cell death under serum depletion.

Gene knockout and knockdown

PI3KC2β-null HEK293 cells were prepared by CRISPR-CAS9 as described previously (Marat et al., 2017). siRNA-based gene knockdown was performed as reported previously (Wang et al., 2009). HEK 293 cells were grown to 30-40% confluency and transfected with various siRNA's

using the JetPRIME system (Polyplus-transfection) according to the manufacturer's protocol. After cells were incubated with siRNA's for 48 h and the suppressed expression level of a target protein was confirmed, they were used for further analysis.

Western blot Analysis

Cells were seeded at a density of 3.0 x 10^5 cells/well 24 h prior to various treatments. After treatments, cells were lysed in the NP40 lysis buffer (50 mM Tris, pH 7.5, 150 mM NaCl, 1 mM EDTA, 1% NP40, 10% glycerol, 10 mM NaF, 10 mM Na3VO4, and protease inhibitor cocktail, pH = 7.4) at 4°C and the mixture cleared by centrifugation. Samples were analyzed by SDS-PAGE. Proteins were separated and transferred to Immobilon-P PVDF membrane (0.45 μm, Millipore Sigma). The membrane was blocked with 5% bovine serum albumin for 1 h and incubated overnight at 4°C with various antibodies (1:500 dilution for the PIKfyve antibody and 1:1000 dilution for all other antibodies). After the unbound antibodies were removed by washing with 0.1% Tris buffer saline with 0.1% Tween20, the membranes were incubated with the horseradish peroxidase secondary antibody (1:2000 dilution) for 1 h at room temperature. The membranes were washed three more times with 0.1% Tris buffer saline with 0.1% Tween20 to remove the unbound horseradish peroxidase secondary antibody before imaging. The chemiluminescence intensity of protein bands in the gel was analyzed and documented by the Azure 500Q Imaging System.

Single-molecule imaging analysis

Single-molecule imaging was performed using a custom-built total internal reflection fluorescence (TIRF) microscope. Mouse embryonic fibroblast (MEF) cells were treated with p85α and p85β siRNA's and then plated on the 8-well chambered cover glass at the density of 1 x 10^5 for 24 h, and EGFP-tagged-p110α and p85α (WT or K653A, respectively) were co-transfected into cells using the jetPRIME system (Polyplus-transfection) according to the manufacturer's protocols. 800 nM YM201636 (24 h) was used to inhibit PIKFyve. Before and after stimulation with 50 ng/ml PDGF-BB, the EGFP signal on the PM was tracked for a given time and the data were analyzed as described previously (Koyama-Honda et al., 2005). All single molecule tracking, data analysis and image processing were carried out with in-house programs written in MATLAB. The PM dissociation rate constant (k) was determined by the non-linear least-squares using a single

exponential decay equation (i.e., $I = I_0 \times e^{-kt}$ where I and I_0 indicate the membrane fluorescence intensity and the maximal I, respectively). The PM dwell time was then expressed as the half-life of dissociation (= $ln2/k$). >250 images from 5 independent measurements were analyzed for every data point.

Colocalization analysis of endogenous PI3K with organelle makers

The same number (1×10^4) of HEK293 cells were seeded onto 24-well plate-compatible coverslips and grown at 37 °C in a humidified atmosphere of 5% CO_2 for about 24 h. Cells were washed twice with phosphate buffer saline (PBS) and then fixed in fresh 4% paraformaldehyde for 10 min, followed by 5 min incubation in 100 mM glycine in PBS to quench the fixation, and further washed twice with PBS, each time for 5 min The cells were then permeabilized with 0.1% (w/v) Triton X-100 in PBS at room temperature for 15 min, followed by treatment with the blocking buffer (5% (v/v) BSA in PBS) at room temperature for 30 min. Cells were incubated with the primary antibodies (1:200 diluted) against PI3K (p110α or p85) and an organelle marker (LAMP1 or EEA1) in PBS (with 1% BSA) overnight at 4℃. Cells were then washed 4 times with PBS, each time for 5 min, and incubated with the secondary antibodies (Goat anti-Mouse Alexa Fluor™ 488 and Goat anti-Rabbit Alexa Fluor™ 568) (1:200 diluted in PBS with 1% BSA) for 2 h at room temperature. Cells were washed 4 times with PBS, each time for 5 min, and used for imaging. Imaging was performed with the custom-designed six channel Olympus FV3000 confocal microscope. Imaging data were analysed using ImageJ (FIJI, ImageJ 1.53t, with Coloc2 (3.0.5) plugin for colocalization analysis). The degree of colocalization was expressed in terms of Pearson's correlation coefficient (R) (Adler and Parmryd, 2013), which was calculated from > 20 cells. The degree of PM localization of PI3K was calculated as $I_{PM}/(I_{PM} + I_{cytosol})$ where I_{PM} and $I_{cytosol}$ indicated the fluorescence intensity at the PM and cytosol, respectively.

Expansion microscopy imaging

The same number (1×10^4) of HEK 293 cells were seeded onto 24-well plate-compatible coverslips and grown at 37°C in a humidified atmosphere of 5% CO_2 for about 24 h. Cells were washed twice with PBS and then fixed in fresh 4% paraformaldehyde for 10 min. The cells were then washed with 100 mM glycine in PBS for 5 min to quench the fixation, and twice with PBS, each time for 5 min. Expanded cells were prepared using a protein-retention expansion microscopy (ExM)

protocol with minor changes (Asano et al., 2018; Tillberg et al., 2016). Briefly, the fixed cells were permeabilized with 0.1% (w/v) Triton X-100 in PBS at room temperature for 15 min and washed with the blocking buffer [5% (v/v) normal goat serum (NGS, Jackson ImmunoResearch) and 0.1% (w/v) Triton X-100 in PBS] at room temperature for 15 min. The cells were then incubated with the primary antibody solution (rabbit anti-p85 antibody with 1:50 dilution and mouse anti-LAMP1 antibody with 1:100 dilution in the blocking buffer) overnight at 4℃. The next day, the cells were washed 4 times with the blocking buffer for 5 min each time, and incubated with the secondary antibody solution (goat anti-mouse Alexa Fluor 488 and goat anti-rabbit Alexa Fluor 568 with1:100 dilution in the blocking buffer) for 2 h at room temperature. Then cells were washed 4 times with PBS, each time for 5 min, and incubated with Acryloyl-X SE solution (0.1 mg/ml in PBS) for 3 h at room temperature. Afterwards, the cells were washed twice with PBS, each time for 15 min, and incubated in a gelling solution prepared by mixing monomer solution [1x PBS, 2 M NaCl, 8.6% (w/v) sodium acrylate (Pfaltz&Bauer), 2.5% (w/v) acrylamide, 0.15% (w/v) N,N'-Methylenebisacrylamide], ammonium persulfate (APS) [10% (w/v)], tetramethylethylenediamine (TEMED) [10% (w/v)], and 4-hydroxy-2,2,6,6-tetramethylpiperidin-1-oxyl (4HT) [0.5% (w/v)] at a 47:1:1:1 ratio. The cells were polymerized in an incubator at 37°C for 1 h, and then the gelled cells were digested overnight at room temperature with digestion buffer [1 mM EDTA, 0.5% Triton X-100, 0.05 M Tris-Cl, 1 M NaCl and 8 units/ml Proteinase K (New England Biolabs) in 1x PBS]. The gelled samples were washed and expanded 3 times with pure water, each time for 20 min. Finally, the expanded samples were trimmed and immobilized on Corning cover glasses (No.1.5) using the poly-L-lysine mounting method for imaging (Asano et al., 2018). Imaging was performed with the custom-designed six channel Olympus FV3000 confocal microscope using DAPI, Alexa Fluor 488 and Alexa Fluor 568 channels. Image data analysis was performed as described above for confocal images.

Calibration of PI(3)P, PI(3,5)P_2, and PIP_3 sensors

In vitro calibration of WCB-*e*p85α-cSH2 was performed with late endosome-mimicking GUVs (POPC/POPE/POPS/cholesterol/PI/PI(3,5)P_2 (20-x/40/20/10/10/*x*: *x* = 0-2 mol%)) or POPC/POPS/PI(3,5)P_2 (77/20/3) as described previously (Liu et al., 2017). GUVs were mixed with the lipid sensors (200 nM) and fluorescence imaging was performed with the custom-designed six channel Olympus FV3000 confocal microscope with the environmentally controlled

full enclosure incubator (CellVivo). WCB-*e*p85α-cSH2 was excited with the 405 nm laser source and the emission intensity was collected in two separate channels with the spectral detector setting of 435-465 nm (blue channel) and 495-525 nm (green channel). For each lipid concentration, at least 30 GUVs were selected for image analysis by Image-Pro Plus7. Calibration curve fitting for WCB-*e*p85α-cSH2 was performed by non-linear least-squares analysis using the equation: $F_B/F_G = (F_B/F_G)_{min} + ((F_B/F_G)_{max} - (F_B F_G)_{min}) / (1 + K_d /[PI(3,5)P_2])$. F_B/F_G, K_d, $(F_B/F_G)_{max}$, and $(F_B/F_G)_{min}$ are the ratio of the fluorescence intensity in the blue channel to that in the green channel, equilibrium dissociation constant (in mol%), and the maximal and minimal F_B/F_G values, respectively (Liu et al., 2017). Calibration of DAN-*e*EEA1 was performed using early-endosome-mimicking GUVs. Calibration of DAN-*e*MyoX-tPH was performed as described (Liu et al., 2018).

In situ quantitative imaging

The same number (2.5 x 10^4) of cells were seeded into Corning cover glasses and grown at 37 °C in a humidified atmosphere of 5% CO_2 in phenol red-free DMEM supplemented with 10% (v/v) FBS, 100 U/ml penicillin G, and 100 mg/ml streptomycin sulfate and cultured in the plates for about 24 h before lipid quantification. Imaging was performed with the custom-designed six channel Olympus FV3000 confocal microscope with the environmentally controlled full enclosure incubator (CellVivo). Cells were maintained at 37°C and with 5% CO_2 atmosphere throughout the imaging period to maintain the cell viability. Typically, 20–30 femtoliter of the sensor solution was microinjected into the cell to reach the final cellular concentration of 200-400 nM. All image acquisition and imaging data analysis were performed as described for GUV calibration. All lipid determination was performed using the GUV calibration curves as described previously (Liu et al., 2017). The three-dimensional display of local lipid concentration profile was calculated using the Surf function in MATLAB.

Quantification and statistical analysis

Statistical analysis was performed using Synergy Kaleidagraph v.5.0. All data are presented as mean ± SD and were obtained from ≥ 3 independent experiments. Statistical significance was calculated by the unpaired Student's t-test (ns, $p > 0.05$; *, $p < 0.05$; **, $p < 0.01$; ***, $p < 0.001$). The number of independent experiments, the number of total cells analyzed, and p values are

reported in the figure legends. Sample sizes for cellular imaging and assays were chosen as the minimum number of independent observations required for statistically significant results.

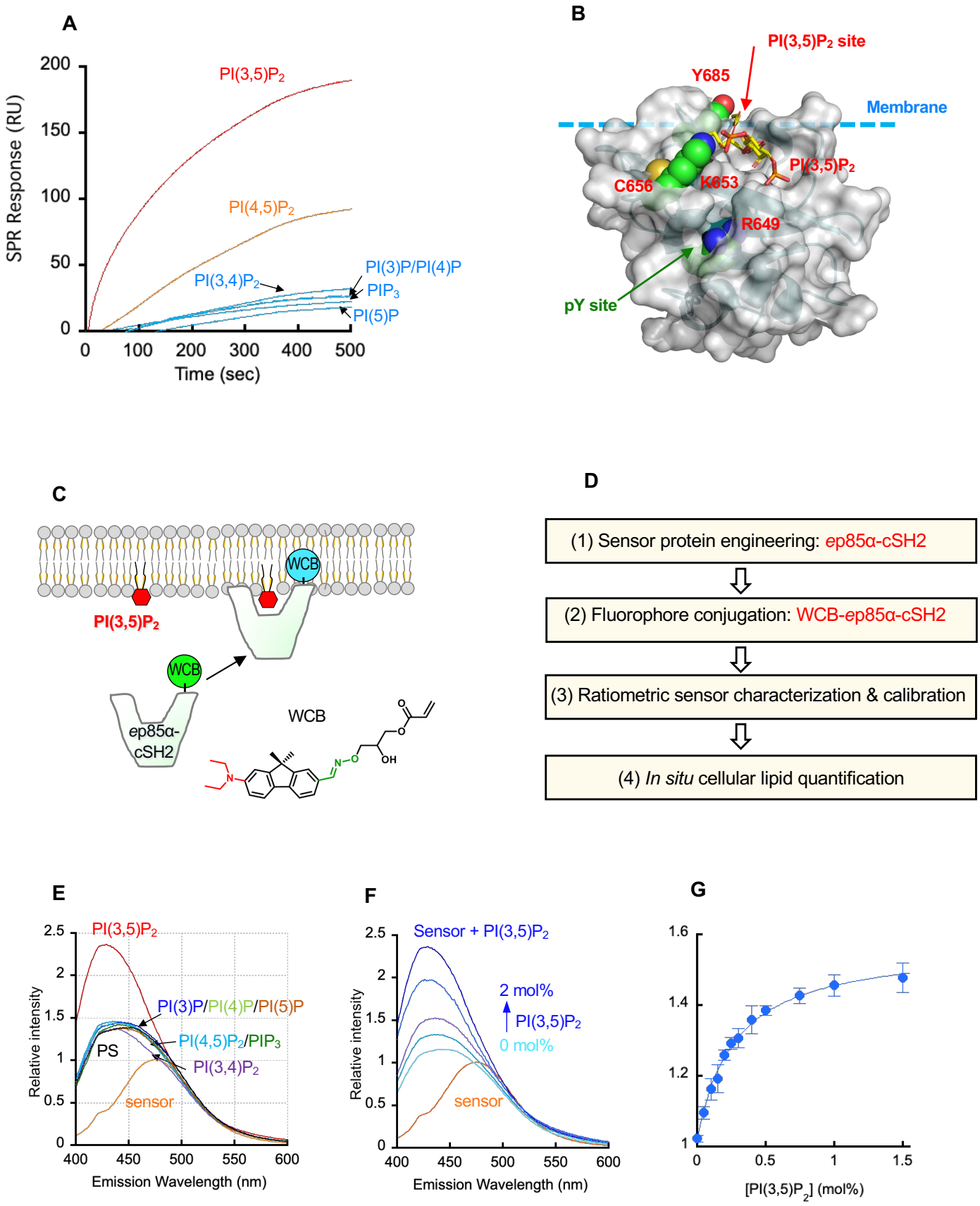
A
SPR Response (RU)
Time (sec)
PI(3,5)P2
PI(4,5)P2
PI(3,4)P2
PI(3)P/PI(4)P
PIP3
PI(5)P
B
PI(3,5)P2 site
Y685
Membrane
PI(3,5)P2
C656
K653
R649
pY site
C
PI(3,5)P2
WCB
ep85α-cSH2
WCB
D
(1) Sensor protein engineering: ep85α-cSH2
(2) Fluorophore conjugation: WCB-ep85α-cSH2
(3) Ratiometric sensor characterization & calibration
(4) In situ cellular lipid quantification
E
Relative intensity
Emission Wavelength (nm)
PI(3,5)P2
PI(3)P/PI(4)P/PI(5)P
PI(4,5)P2/PIP3
PS
PI(3,4)P2
sensor
F
Relative intensity
Emission Wavelength (nm)
Sensor + PI(3,5)P2
2 mol%
PI(3,5)P2
0 mol%
sensor
G
[PI(3,5)P2] (mol%)

Fig. 1

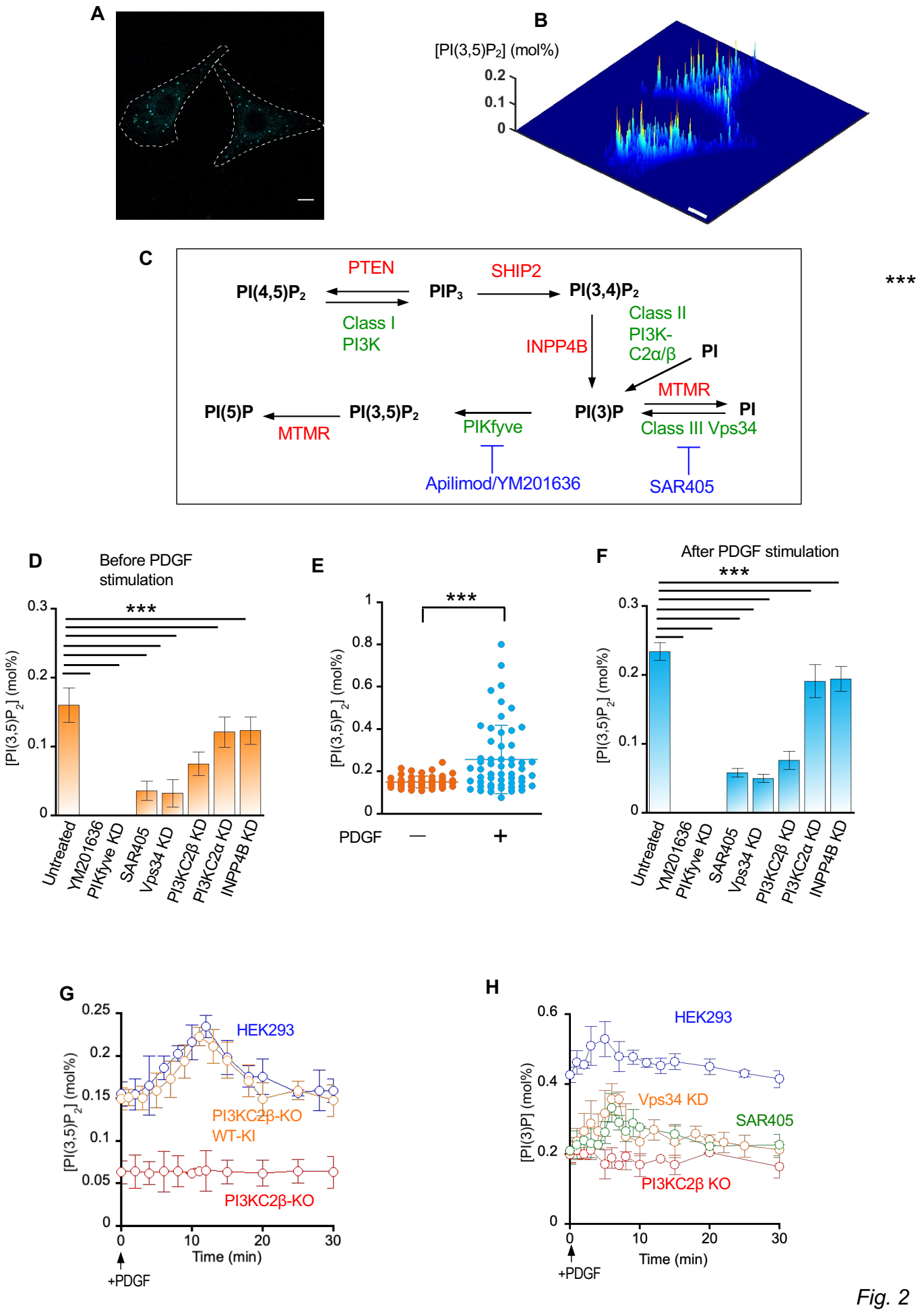
A
B
[PI(3,5)P2] (mol%)
0.2
0.1
0
C
PTEN
SHIP2
PI(4,5)P2
PIP3
PI(3,4)P2
Class I PI3K
Class II PI3K-C2α/β
INPP4B
PI
MTMR
PI(5)P
PI(3,5)P2
PI(3)P
PI
MTMR
PIKfyve
Class III Vps34
Apilimod/YM201636
SAR405
***
D
Before PDGF stimulation
***
[PI(3,5)P2] (mol%)
Untreated
YM201636
PIKfyve KD
SAR405
Vps34 KD
PI3KC2β KD
PI3KC2α KD
INPP4B KD
E
***
PDGF
—
+
F
After PDGF stimulation
***
G
HEK293
PI3KC2β-KO
WT-KI
PI3KC2β-KO
Time (min)
+PDGF
H
HEK293
Vps34 KD
SAR405
PI3KC2β KD
[PI(3)P] (mol%)
Time (min)
+PDGF

Fig. 2

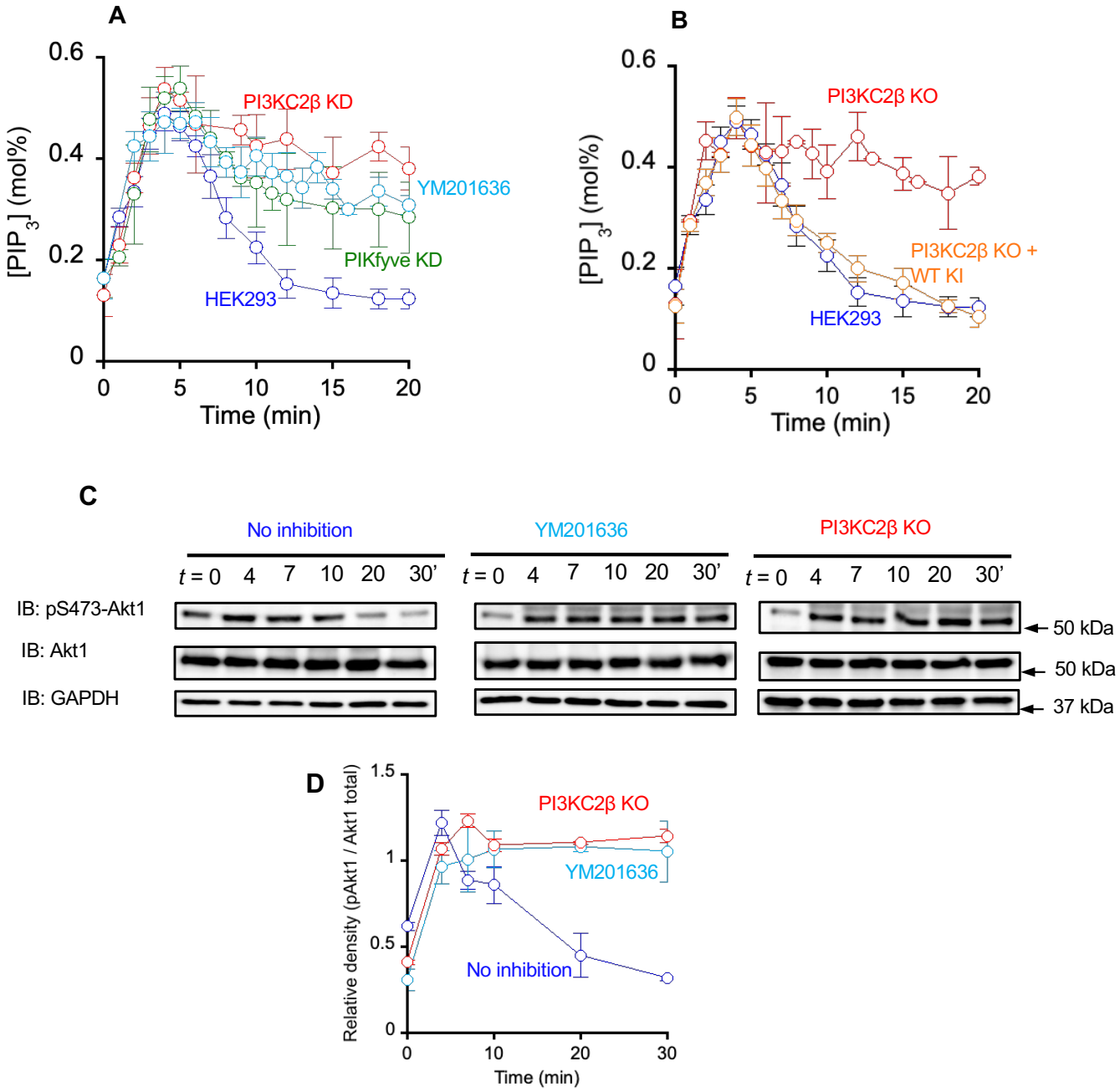
A
0.6
0.4
0.2
0
[PIP3] (mol%)
PI3KC2β KD
YM201636
PIKfyve KD
HEK293
0
5
10
15
20
Time (min)
B
0.6
0.4
0.2
0
[PIP3] (mol%)
PI3KC2β KO
PI3KC2β KO +
WT KI
HEK293
0
5
10
15
20
Time (min)
C
No inhibition
YM201636
PI3KC2β KO
t = 0 4 7 10 20 30'
t = 0 4 7 10 20 30'
t = 0 4 7 10 20 30'
IB: pS473-Akt1
IB: Akt1
IB: GAPDH
50 kDa
50 kDa
37 kDa
D
1.5
1
0.5
0
Relative density (pAkt1 / Akt1 total)
PI3KC2β KO
YM201636
No inhibition
0
10
20
30
Time (min)

Fig. 3

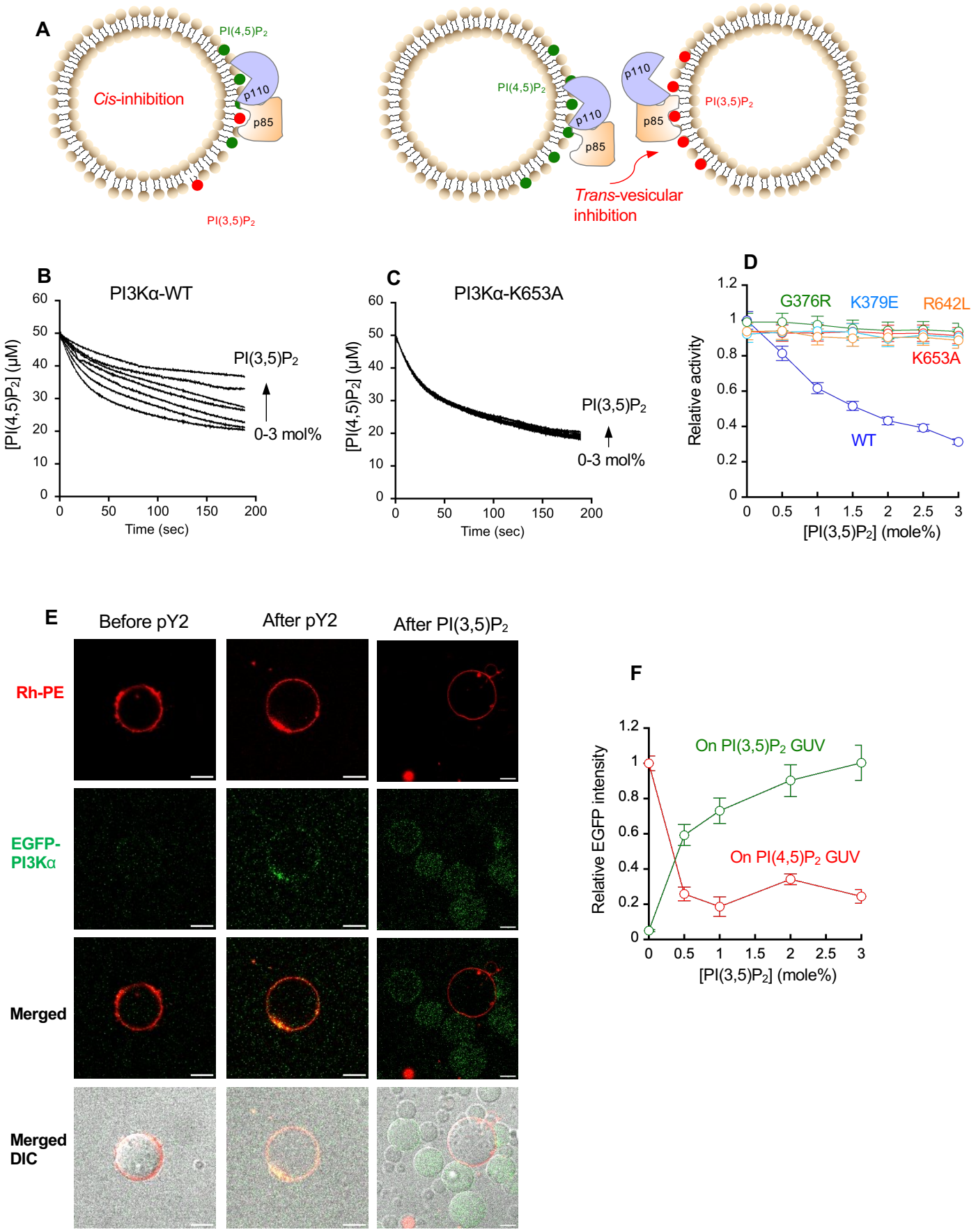
A
PI(4,5)P2
Cis-inhibition
p110
p85
PI(3,5)P2
PI(4,5)P2
p110
p85
p110
p85
PI(3,5)P2
Trans-vesicular
inhibition
B
PI3Kα-WT
[PI(4,5)P2] (μM)
PI(3,5)P2
0-3 mol%
Time (sec)
C
PI3Kα-K653A
[PI(4,5)P2] (μM)
PI(3,5)P2
0-3 mol%
Time (sec)
D
G376R
K379E
R642L
K653A
WT
Relative activity
[PI(3,5)P2] (mole%)
E
Before pY2
After pY2
After PI(3,5)P2
Rh-PE
EGFP-
PI3Kα
Merged
Merged
DIC
F
On PI(3,5)P2 GUV
On PI(4,5)P2 GUV
Relative EGFP intensity
[PI(3,5)P2] (mole%)

Fig. 4

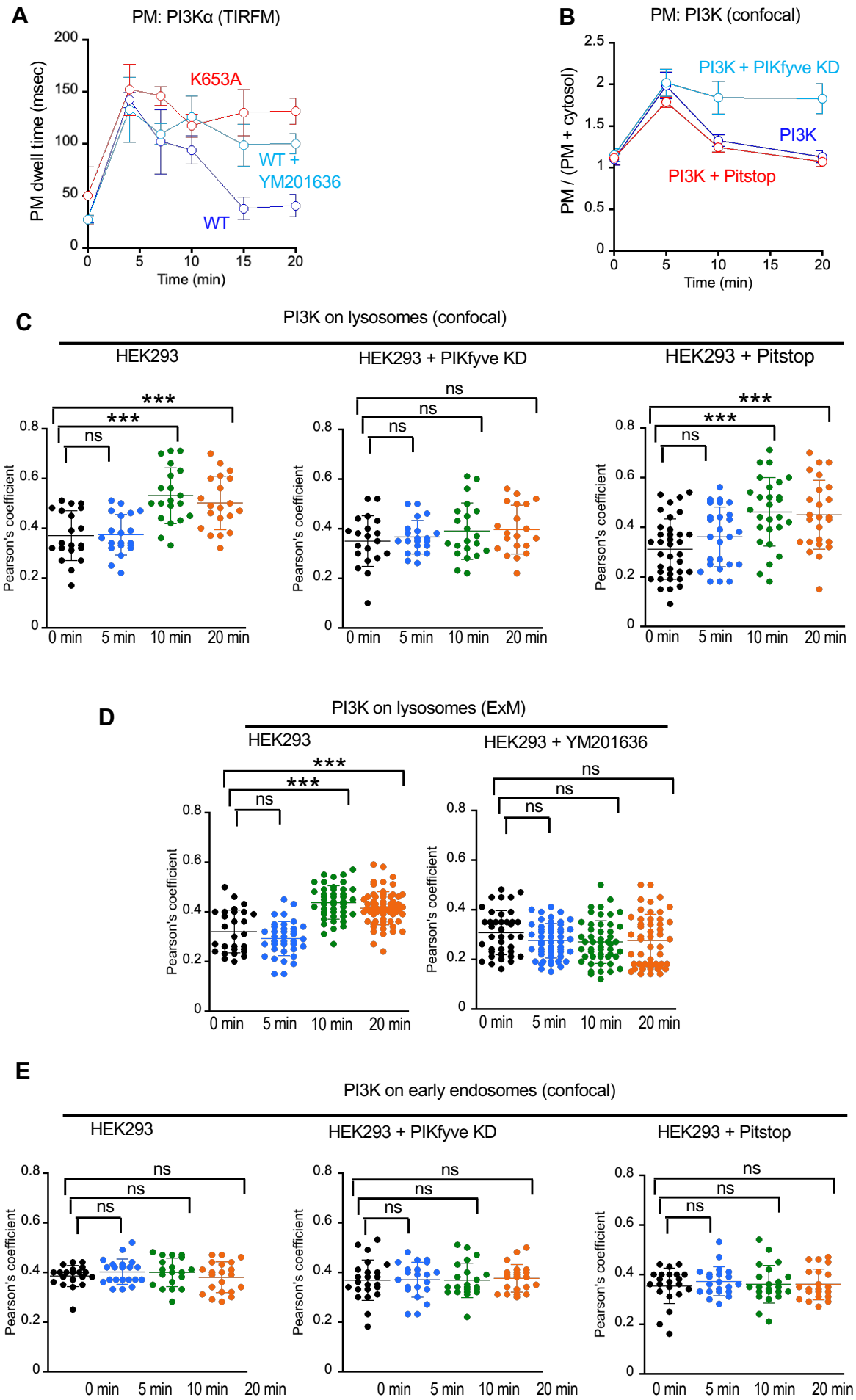
A
PM: PI3Kα (TIRFM)
PM dwell time (msec)
Time (min)
K653A
WT + YM201636
WT
B
PM: PI3K (confocal)
PM / (PM + cytosol)
Time (min)
PI3K + PIKfyve KD
PI3K
PI3K + Pitstop
C
PI3K on lysosomes (confocal)
HEK293
HEK293 + PIKfyve KD
HEK293 + Pitstop
Pearson's coefficient
0 min
5 min
10 min
20 min
ns
***
D
PI3K on lysosomes (ExM)
HEK293
HEK293 + YM201636
E
PI3K on early endosomes (confocal)
HEK293
HEK293 + PIKfyve KD
HEK293 + Pitstop

Fig. 5

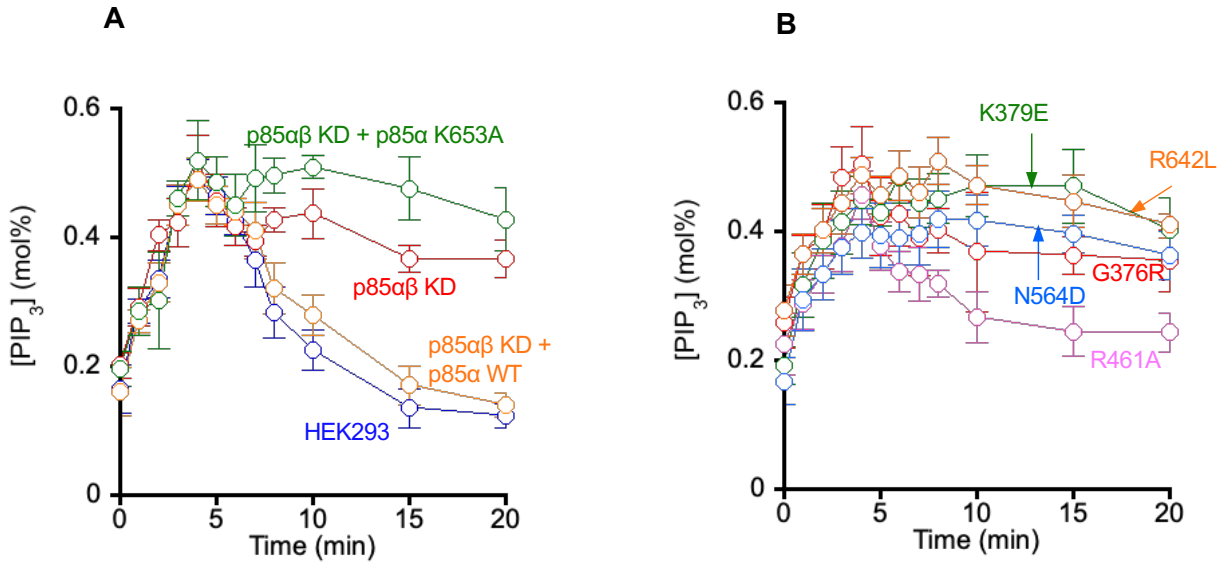
A
B
0.6
0.4
0.2
0
[PIP3] (mol%)
0
5
10
15
20
Time (min)
p85αβ KD + p85α K653A
p85αβ KD
p85αβ KD +
p85α WT
HEK293
K379E
R642L
G376R
N564D
R461A

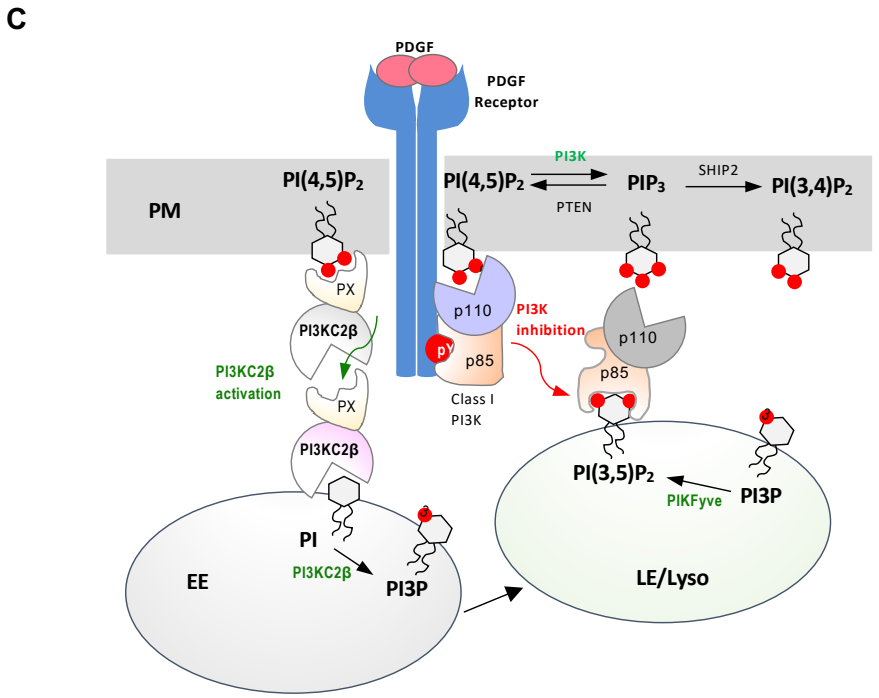
C
PDGF
PDGF
Receptor
PM
PI(4,5)P2
PI3K
PI(4,5)P2
PIP3
SHIP2
PI(3,4)P2
PTEN
PX
PI3KC2β
PI3KC2β
activation
PX
PI3KC2β
p110
p85
Class I
PI3K
PI3K
inhibition
p110
p85
PI
PI3KC2β
PI3P
EE
PI(3,5)P2
PIKFyve
PI3P
LE/Lyso

Fig. 6